Forced internal wave attractors: Linear inviscid theory

Zakhar V. Makridin [1,*] Alexander K. Khe [1]
Ilias N. Sibgatullin [2,3] and Eugeny V. Ermanyuk [1]

[1]*Lavrentyev Institute of Hydrodynamics, 630090 Novosibirsk, Russia*
[2]*School of Computer Science and Mathematics, Keele University, Staffordshire, ST5 5AA, United Kingdom*
[3]*Univ Lyon, ENS de Lyon, CNRS, Laboratoire de Physique, F-69342 Lyon, France*

In this paper, we study internal wave focusing in a trapezoidal domain with one moving boundary. Using linear theory, we construct an exact analytic solution for the case of ideal uniformly stratified Boussinesq fluid, which is appropriate for developing weakly nonlinear theory. This analytical solution is compared against the results of direct numerical simulations performed with the help of the spectral element method. It is shown that the nested structure of wave beams in the ideal-fluid solution is consistent with the peculiarities of the wave-beam profiles obtained in weakly viscous numerical simulations performed in a range of Stokes numbers covering three orders of magnitude beyond the typical experimental values. Finally, we explore the role of the shape of the wave generator on the instantaneous profiles and envelopes of the wave beams.

I. INTRODUCTION

Within the linear theory of a uniformly stratified, nonrotating, incompressible, inviscid two-dimensional Boussinesq fluid, it can be easily shown that spatial structure of internal monochromatic wave stream function $\Psi(x, z, t) = \text{Re}\{\psi(x, z)e^{-i\omega t}\}$ is governed by hyperbolic wave equation for $\psi(x, z)$ with prescribed values on the boundary [1–3]. The solution of this Dirichlet problem can be represented by the mapping of the boundary on itself (see, e.g., Refs. [4–6] for relevant mathematical aspects). Specifically, given a single point on the boundary, its images can be defined by forward and backward iteration of the mapping correspondingly, following the characteristic lines passing through that point both in rightward and leftward directions. Thus, one can construct a web of wave rays iteratively and then specify the stream-function value at each point of the domain. Under the appropriate choice of parameters, wave attractors arise by construction as closed orbits, accumulating wave energy, injected from the boundary of the closed domain.

This procedure was used in Ref. [7], where the stream-function field of an unforced standing wave attractor was obtained and some properties of the mapping were discussed. Later, in Ref. [8], an internal wave attractor was observed experimentally around a theoretically predicted location in a trapezoidal setup. Also, it was pointed out that the wave field initially behaves as a standing wave and tends to a stationary state on the form of a propagating wave. Thus, there is some inconsistency with the experiment, since theory [7] describes the standing-wave solution only. This issue was studied in Ref. [9], where a traveling wave solution for sloshing-type surface forcing was obtained (also iteratively), allowing one to apply more realistic boundary conditions.

Iterative construction of a solution is inappropriate for subsequent development of a weakly nonlinear theory, since the wave field is defined pointwise. An analytic solution of a standing

---

*makridin@hydro.nsc.ru

wave attractor was given in Ref. [10], where the wave field in a 2D trapezoidal domain was represented as a Fourier series with coefficients satisfying the functional equation, which results in log periodicity of the spectrum. Such functional equations were further investigated in Ref. [11] within the framework of internal wave theory in confined domains.

The linear theory of weakly viscous forced internal wave attractor was developed in Refs. [12,13]. With this approach, the forcing is defined as a localized source, located outside of the trapezoidal domain. Then, the wave attractor is constructed as four branches of a viscous internal wave beam, reflected at vertical and horizontal boundaries, and closed on itself at the sloping wall. This requires the spectrum to satisfy the appropriate functional equation, similar to Ref. [10]. Accordingly, one can construct a wave attractor with any spectrum satisfying the corresponding functional equation. Thus, it is not obvious how to relate the spectrum of a localized source with that of a moving boundary. In some cases, such a relation can be disregarded. For example, the scaling law governing the equilibrium width of the wave beams in a weakly viscous fluid can be obtained under the assumption that the geometric focusing is balanced by viscous diffusion, while the wave beams are represented by free self-similar oblique shear layers in the spirit of Ref. [14]. In a more systematic way, this approach requires the solution of the linearized boundary-layer-type equations for free shear layers representing the attractor beams. There exists rich literature on this approach in application to inertial waves in rotating spherical shells [15,16] (see also Ref. [17]), where a similar approach is used). The scaling law obtained with this approach is in reasonable agreement with the available data in the vicinity of the wave-ray skeleton of the attractor [18]. However, such an approach does not consider any relation to a specific form of forcing imposed at the boundary of the liquid domain. In addition, such an approach does not consider a link between the inner solution (understood as a specific free shear boundary layer) and the outer solution for the background wave motion in the fluid bulk external to the boundary layer.

In the present paper, we develop the linear theory of an inviscid forced internal wave attractor in a 2D trapezoidal domain, with one moving wall. This classic setup has been studied theoretically [7,8], experimentally [8,18,19], and numerically [20,21] as a model problem possessing rich nonlinear dynamics which mimics some essential features of internal wave climate in natural stratified basins [22]. Our goal is to fill some gaps in the understanding of the global wave-field structure of wave attractors. In particular, we explore how the nested structure of the inviscid solution corresponding to different profiles of the forcing imposed at the moving boundary is inherited by a weakly viscous numerical solution at different values of viscosity, including typical laboratory conditions. Moving walls undergoing prescribed motion are getting increasingly popular in experiments to inject energy in wave attractors [19,23] as compared to a more traditional approach with inertial sloshing-type forcing [8,24]. The inviscid theory of such moving-wall generators is relatively straightforward in application to the wave beams in unbounded domains [25,26], while the problem remains open for bounded domains.

II. GOVERNING EQUATIONS

We consider inviscid, incompresssible, uniformly stratified, nonrotating Boussinesq fluid, filling a two-dimensional right-angled trapezoidal domain Ω of height H and length h [see Fig. 1 (left)]. A sloping wall is inclined at an angle α with respect to the horizontal. Equations of motion can be written as

$$\mathbf{u}_t + (\mathbf{u} \cdot \nabla)\mathbf{u} = -\frac{1}{\rho_*}\nabla p + \mathbf{e}_z b, \tag{1}$$

$$b_t + \mathbf{u} \cdot \nabla b = -vN^2, \tag{2}$$

$$\nabla \cdot \mathbf{u} = 0, \tag{3}$$

where $\nabla = (\partial_x, \partial_z)$, $\mathbf{e}_z = (0, 1)$, $\mathbf{u} = (u, v)$ is the fluid velocity field, ρ_* is the characteristic density of the fluid (averaged over the stratified region), such that fluid density at rest is $\rho_* + \rho_0(z)$, p
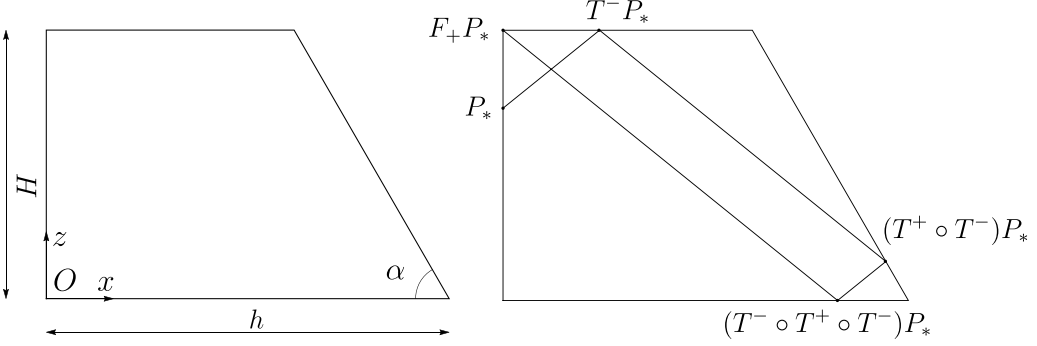
FIG. 1. Left: Schematic view of the two-dimensional trapezoidal domain. The coordinate origin O is placed at the bottom left vertex. Right: Forward evolution of the point P_* under characteristic map.

is the pressure fluctuation with respect to the hydrostatic equilibrium $dp_0/dz = -g(\rho_* + \rho_0(z))$, $b = -g\rho'/\rho_*$ the perturbed buoyancy field with g being gravitational constant and $N^2(z) = -(g/\rho_*)d\rho_0/dz$ the buoyancy frequency. Continuity Eq. (3) allows us to introduce stream function $\Psi(x, z, t)$, such that $u = \Psi_z$, $v = -\Psi_x$. Then the linearized system Eqs. (1) and (2) transform to

$$\nabla^2\Psi_t = -b_x, \quad b_t = \Psi_x,$$

which, under elimination of b, leads to the following linear partial differential equation of Sobolev type [27]:

$$\nabla^2\Psi_{tt} + \Psi_{xx} = 0. \tag{4}$$

Here we take $N = 1$ for simplicity. Equations similar to Eq. (4) were studied in Refs. [5,28–30] in the framework of spectral theory and more recently in Refs. [31–33] in the context of inertial and internal wave attractors with a forcing term added the right-hand side. After the substitution $\Psi(x, z, t) = \psi(x, z)e^{-i\omega t}$, Eq. (4) reduces to the wave equations

$$\psi_{xx} - \lambda^2\psi_{zz} = 0, \quad \lambda^2 = \frac{\omega^2}{1 - \omega^2}. \tag{5}$$

It admits a plane-wave solution with wave vector $\mathbf{k} = (m, l)$ and wave number $|\mathbf{k}| = (m^2 + l^2)^{1/2}$ if and only if the dispersion relation

$$\omega = \pm m/|\mathbf{k}| = \pm\sin\theta \tag{6}$$

is satisfied. Here θ is the angle between the wave vector $\mathbf{k}$ and the vertical, therefore $\lambda^2 = \tan^2\theta$. We use free slip conditions on the boundary $\partial\Omega$:

$$\psi_z|_{x=0} = U(z), \quad \psi_x|_{z=0} = \psi_x|_{z=H} = 0, \quad \{\psi_z\tan\alpha - \psi_x\}|_{z=\tan\alpha(h-x)} = 0, \tag{7}$$

with the given real-valued function $U(z)$. Note that the stream function Ψ admits representation

$$\Psi(x, z, t) = \text{Re}\{\psi(x, z)e^{-i\omega t}\} = \varphi(x, z)\cos\omega t + \eta(x, z)\sin\omega t,$$

where Re denotes the real part. Therefore, real φ and imaginary η parts of complex amplitude ψ are equal to the stream function Ψ at $t = t_*$ and $t = t_{**}$, respectively:

$$\Psi(x, z, t_*) = \varphi(x, z), \quad t_* = \frac{2\pi k}{\omega}, \quad k = 0, 1, 2, \dots,$$

$$\Psi(x, z, t_{**}) = \eta(x, z), \quad t_{**} = \frac{\pi}{2\omega} + \frac{2\pi k}{\omega}, \quad k = 0, 1, 2, \dots.$$
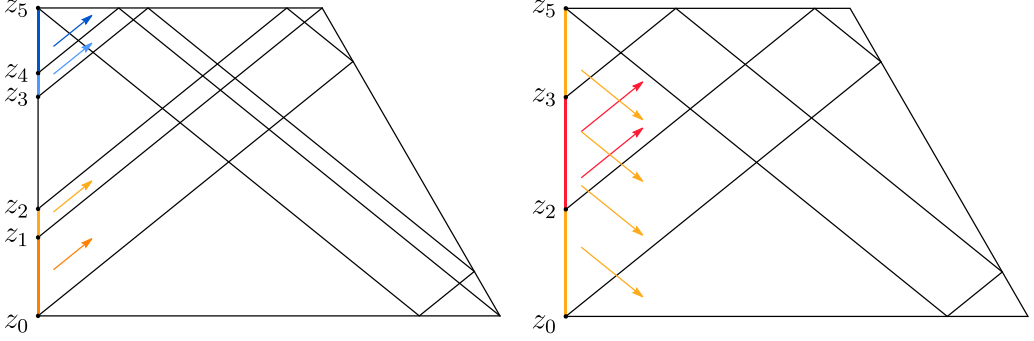
FIG. 2. Left: Wave rays, propagating upward from the intervals $[z_0, z_2]$ and $[z_3, z_5]$. Right: Wave rays, propagating upward from the interval $[z_2, z_3]$, and downward from $[z_0, z_5]$.

III. WEB OF WAVE RAYS

For further investigation, one needs to build up web of wave rays. Let us define two maps $T^\pm$ in the following way [see Fig. 1 (right)]: each point $P_* = (x_*, z_*) \in \partial\Omega$ is mapped to $T^+P_* = (x_+, z_+)$ and $T^-P_* = (x_-, z_-)$ obtained as an intersection of corresponding characteristics with the boundary $\partial\Omega$. To get the coordinates of $T^\pm P_*$, one should solve the following system:

$$x_\pm \pm \lambda^{-1}z_\pm = x_* \pm \lambda^{-1}z_*$$
$$T^\pm P_* \in \partial\Omega.$$

Now, consider two sequences:

$$S_\pm(P_*) = \{P_*, \ T^\pm P_*, \ (T^\mp \circ T^\pm)P_*, \ (T^\pm \circ T^\mp \circ T^\pm)P_*, \ \ldots\}.$$

The sequence $S_+(P_*)$ $(S_-(P_*))$ can be considered as forward (backward) evolution of the point P_* under some map, which is called the characteristic map. Denote by $L_\pm(P_*)$ a set of characteristics, connecting any two successive points of $S_\pm(P_*)$. Since the forcing is prescribed on the $\{x = 0, z \in [0, H]\} = \Gamma \subset \partial\Omega$, then, following Ref. [9], the wave ray web is defined as

$$\mathrm{WR}(\Omega) = \bigcup_{P_* \in \Gamma} L_\pm(P_*).$$

After a close look at the wave ray web, one can observe that rays, starting from different points on the Γ, reflect differently. Specifically, let us introduce the set

$$O_\Gamma^\pm(P_*) = S_\pm(P_*) \cap \Gamma,$$

called the Γ orbit of point P_* under forward (+) or backward (−) iteration of the characteristic map. For a given point $P_* \in \Gamma$ with coordinates $(0, z_*)$, consider the following six cases (see Fig. 2):

(I) For $z_* \in [z_0, z_5]$, where $z_0 = 0, z_5 = H$ (see Fig. 2), we have

$$O_\Gamma^-(P_*) = \{P_*, \ F_-P_*, \ F_-^2 P_*, \ F_-^3 P_*, \ \ldots\},$$

with $F_\pm = T^\pm \circ T^\mp \circ T^\pm \circ T^\mp$, corresponding to clockwise (+) or counterclockwise (−) wave ray cycle.

(II) (Singular case.) For $z_* \in [z_2, z_3]$, where $z_2 = 2H - 2h\tan\alpha/(1 + \cot\theta\tan\alpha)$ and $z_3 = 2H - h\tan\alpha - (H + h\tan\alpha)(1 - \cot\theta\tan\alpha)/(1 + \cot\theta\tan\alpha)$, it is readily seen from Fig. 2 that the second point in Γ orbit may fall outside the interval $[z_2, z_3]$. Thus,

$$O_\Gamma^+(P_*) = \{P_*, \ P_{**}, \ O_\Gamma^+(P_{**})\},$$

and one should check subsequent cases to obtain the Γ orbit of $P_{**} = F_+P_*$.

(III) For $z_* \in [z_0, z_1]$ with $z_1 = H - \tan\theta(h - H\cot\alpha)$ (see Fig. 2), we have

$$O_\Gamma^+(P_*) = \{P_*, \ P_{**}, \ F_-P_{**}, \ F_-^2 P_{**}, \ldots\},$$

with $P_{**} = (T^- \circ T^+ \circ T^-)P_*$.

(IV) For $z_* \in [z_1, z_2]$ (see Fig. 2), we have

$$O_\Gamma^+(P_*) = \{P_*, \ P_{**}, \ F_-P_{**}, \ F_-^2 P_{**}, \ldots\},$$

with $P_{**} = (T^- \circ T^+ \circ T^-)P_*;.$

(V) For $z_* \in [z_3, z_4]$, where $z_4 = 2H - h/\cot\theta$, we have

$$O_\Gamma^+(P_*) = \{P_*, \ P_{**}, \ F_-P_{**}, \ F_-^2 P_{**}, \ldots\},$$

with $P_{**} = (T^- \circ F_+)P_*$.

(VI) For $z_* \in [z_4, z_5]$, we have

$$O_\Gamma^+(P_*) = \{P_*, \ P_{**}, \ F_-P_{**}, \ F_-^2 P_{**}, \ldots\},$$

with $P_{**} = (F_- \circ T^+)P_*$.

Thus, one can see that the profile, specified at the Γ, is traced by the wave rays in different ways, according to the six cases written above. The first case shows that the profile focuses under the backward iteration of the characteristic map. Cases III–VI show that after several reflections, wave rays tend to the focusing regime described by case I. Finally, the singular case represents defocusing part of the initial profile.

It is worth noting that cases III and IV seem to be the same, but it is not the case, as will be seen from the solution. The similar situation stands for cases V and VI: we formally defined P_{**} in two different ways to emphasize that corresponding solutions differ from each other (see Appendix).

IV. SOLUTION CONSTRUCTING

Suppose we are dealing with internal waves propagation in an infinite domain. Since the dispersion relation Eq. (6) defines frequency ω independent of the wave number, one can superimpose plane-wave solutions with different wave numbers $|\mathbf{k}|$, propagating at the same angle θ. Thus, we may represent a solution in the form of Fourier integrals:

$$\psi(x, z) = \int_0^{+\infty} e^{im_1(l)x}\{\overset{\searrow}{Q}(l)e^{ilz} + \overset{\nearrow}{Q}(-l)e^{-ilz}\}dl + \int_0^{+\infty} e^{im_2(l)x}\{\overset{\swarrow}{Q}(l)e^{ilz} + \overset{\nwarrow}{Q}(-l)e^{-ilz}\}dl. \tag{8}$$

Here $m_{1,2}(l)$ are defined from Eq. (6) and $\overset{\bullet}{Q}(l)$ is the Fourier spectrum of the plane-wave superposition with group velocity direction $\bullet \in \{\nearrow, \searrow, \nwarrow, \swarrow\}$. The solution of the form Eq. (8) contains four unidirectional internal wave beams [34], each transferring energy in one direction only. The weakly nonlinear theory of beam propagation in unconfined domains, including its interaction, stability, mean flow generation, and reflection at sloping boundaries, is well developed (see Refs. [34–45] and references therein).

To construct a solution in trapezoidal domain Ω, one can take an integral solution representation inside the trapezoidal domain, substitute it into boundary conditions, and then solve numerically the integral equation obtained [46–48] (see also references therein). Instead, we consider whole plane $\mathbb{R}^2$ and place virtual sources of localized unidirectional wave beams such that boundary conditions Eqs. (7) are satisfied. This scheme allows us to use Fourier transform and, consequently, solution representation Eq. (8). Specifically, we solve the auxiliary boundary value problem in an infinite domain:

$$\psi_{xx} - \lambda^2 \psi_{zz} = 0, \quad \psi_z|_{x=0} = U_H(z) + S_{\text{mov}}(z), \quad \psi_x|_{z=0} = S_{\text{bot}}(x),$$

$$\psi_x|_{z=H} = S_{\text{top}}(x), \quad \{\psi_z \tan\alpha - \psi_x\}|_{z=\tan\alpha(h-x)} = S_{\text{inc}}(x, z)|_{z=\tan\alpha(h-x)}. \tag{9}$$

Here $U_H(z) = \chi_H(z)U(z)$, $\chi_H(z)$ is a characteristic function of the interval $[0, H]$ and S_{mov}, S_{bot}, S_{top}, S_{inc} are source-type terms which will be determined later.

As discussed in the previous section, beams can be separated into six groups. Therefore, it is natural to represent the solution as follows:

$$\psi(x, z) = \psi_{\text{I}}^-(x, z) + \psi_{\text{II}}^+(x, z) + \psi_{\text{III}}^+(x, z) + \psi_{\text{IV}}^+(x, z) + \psi_{\text{V}}^+(x, z) + \psi_{\text{VI}}^+(x, z), \qquad (10)$$

where each term is of the form Eq. (8) and upper index $\pm$ corresponds to the slope sign of wave beam, starting from moving boundary. A similar representation takes place for all source terms in Eq. (9). Since cases II–VI ultimately reduce to case I, we consider the latter in detail. Let us remember the definition of Fourier transform $\widehat{f}$ (together with its inverse) of the integrable function f, which we will use:

$$\widehat{f}(l) = \int_{-\infty}^{+\infty} f(z)e^{-ilz}dz, \quad f(z) = \frac{1}{2\pi}\int_{-\infty}^{+\infty} \widehat{f}(l)e^{ilz}dl.$$

Also, it will be useful to remember the Fourier transform of a product of two integrable functions $f(z)$ and $g(z)$:

$$\widehat{fg}(l) = \frac{1}{2\pi}(\widehat{f} * \widehat{g})(l).$$

A. Solution for case I

Solution is sought in the following form:

$$\psi_{\text{I}}^- = \sum_{k=1}^{\infty} \psi_{k,\text{I}}^-, \quad \psi_{k,\text{I}}^-(x, z) = \int_0^{+\infty} e^{ilx\tan\theta}\{\overset{\searrow}{Q}_{k,\text{I}}(l)e^{ilz} + \overset{\nearrow}{Q}_{k,\text{I}}(-l)e^{-ilz}\}dl$$

$$+ \int_0^{+\infty} e^{-ilx\tan\theta}\{\overset{\swarrow}{Q}_{k,\text{I}}(l)e^{ilz} + \overset{\nwarrow}{Q}_{k,\text{I}}(-l)e^{-ilz}\}dl. \qquad (11)$$

The function ψ_{I}^- must satisfy boundary conditions[see Eq. (9)]:

$$(\psi_{\text{I}}^-)_z|_{x=0} = \frac{1}{2\pi}\int_0^{+\infty} \widehat{U}_H(l)e^{ilz}dl + S_{\text{I,mov}}(z), \quad (\psi_{\text{I}}^-)_x|_{z=0} = S_{\text{I,bot}}(x), \qquad (12)$$

$$(\psi_{\text{I}}^-)_x|_{z=H} = S_{\text{I,top}}(x), \quad \{(\psi_{\text{I}}^-)_z\tan\alpha - (\psi_{\text{I}}^-)_x\}|_{z=\tan\alpha(h-x)} = S_{\text{I,inc}}(x, z)|_{z=\tan\alpha(h-x)}. \qquad (13)$$

Here we took only one piece of Fourier representation,

$$U_H(z) = \frac{1}{2\pi}\int_0^{+\infty} \widehat{U}_H(l)e^{ilz}dl + \frac{1}{2\pi}\int_0^{+\infty} \widehat{U}_H(-l)e^{-ilz}dl, \qquad (14)$$

which corresponds to the downward propagating beam. Consider boundary conditions on the moving wall in detail:

$$\frac{1}{2\pi}\int_0^{+\infty} \widehat{U}_H(l)e^{ilz}dl + S_{\text{I,mov}}(z) = \int_0^{+\infty} il\,\overset{\searrow}{Q}_{1,\text{I}}(l)e^{ilz}dl + \sum_{k=2}^{\infty}\int_0^{+\infty} il\{\overset{\swarrow}{Q}_{k-1,\text{I}}(l) + \overset{\searrow}{Q}_{k,\text{I}}(l)\}e^{ilz}dl$$

$$+ \sum_{k=1}^{\infty}\int_0^{+\infty}(-il)\{\overset{\nearrow}{Q}_{k,\text{I}}(-l) + \overset{\nwarrow}{Q}_{k,\text{I}}(-l)\}e^{-ilz}dl.$$

Our aim is to satisfy boundary conditions on the moving wall from Eqs. (7). It is easy to see that wave beams with Fourier spectra $\overset{\swarrow}{Q}_{k,\text{I}}$ and $\overset{\searrow}{Q}_{k,\text{I}}$ only propagate toward and away from the segment $\Gamma = \{x = 0, z \in [0, H]\}$ for all $k = 1, 2, \dots$ (see Fig. 3). Thus, all other beams must be absorbed by
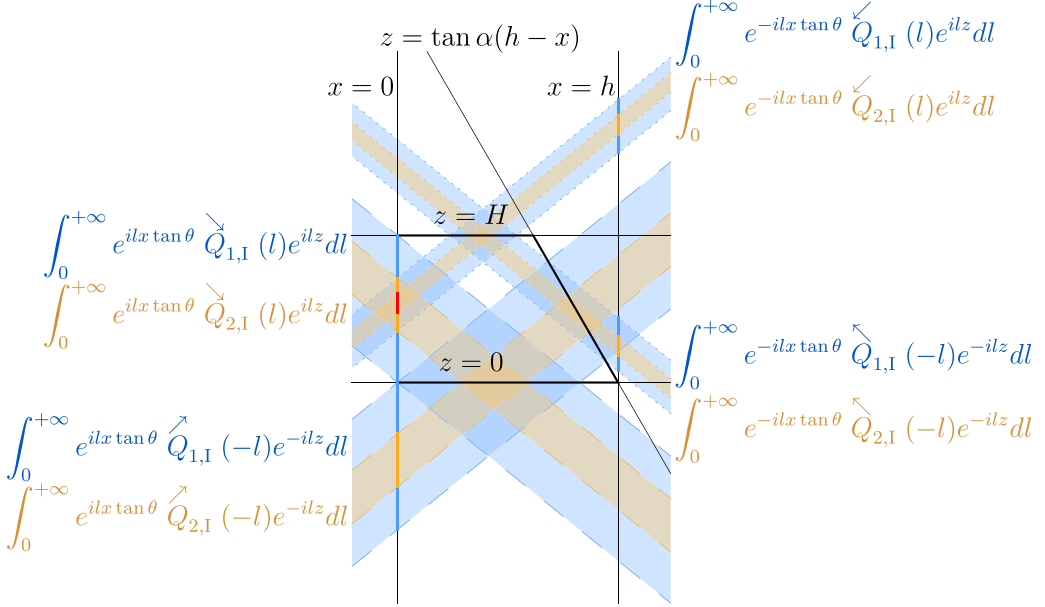
FIG. 3. Virtual sources for the first two iterations are depicted (blue and yellow segments on lines $x = 0$ and $x = h$). Each Fourier integral corresponds to a localized internal wave beam of the same color placed near the integral. Red line denotes the interval where the discrepancy appears when the iterative procedure is interrupted.

the function $S_{\mathrm{I,mov}}$. This results in the following relations:

$$\overset{\searrow}{Q}_{1,\mathrm{I}}(l) = \frac{\widehat{U}_H(l)}{2i\pi l}, \quad \overset{\searrow}{Q}_{k,\mathrm{I}}(l) = -\overset{\swarrow}{Q}_{k-1,\mathrm{I}}(l), \quad k = 2, 3, \ldots,$$

$$S_{\mathrm{I,mov}}(z) = \sum_{k=1}^{\infty} \int_0^{+\infty} (-il)\{\overset{\nearrow}{Q}_{k,\mathrm{I}}(-l) + \overset{\nwarrow}{Q}_{k,\mathrm{I}}(-l)\}e^{-ilz}dl. \tag{15}$$

By similar reasoning, the second boundary condition from Eq. (12) and the first one from Eq. (13) lead to

$$S_{\mathrm{I,bot}}(x) = \sum_{k=1}^{\infty} \int_0^{+\infty} (-il)\tan\theta\{\overset{\swarrow}{Q}_{k,\mathrm{I}}(l) + \overset{\nwarrow}{Q}_{k,\mathrm{I}}(-l)\}e^{-ilx\tan\theta}dl,$$

$$S_{\mathrm{I,top}}(x) = \sum_{k=1}^{\infty} \int_0^{+\infty} il\tan\theta\{\overset{\searrow}{Q}_{k,\mathrm{I}}(l)e^{ilH} + \overset{\nearrow}{Q}_{k,\mathrm{I}}(-l)e^{-ilH}\}e^{ilx\tan\theta}dl,$$

$$\overset{\searrow}{Q}_{k,\mathrm{I}}(l) = -\overset{\nearrow}{Q}_{k,\mathrm{I}}(-l), \quad \overset{\swarrow}{Q}_{k,\mathrm{I}}(l) = -\overset{\nwarrow}{Q}_{k,\mathrm{I}}(-l)e^{-2ilH}, \quad k = 1, 2, \ldots. \tag{16}$$

The second equality in Eq. (13), being condition on the sloping wall, results in the following relations:

$$S_{\mathrm{I,inc}}(x, z) = \sum_{k=1}^{\infty} \Bigg\{ (\tan\alpha - \tan\theta) \int_0^{+\infty} il\, \overset{\searrow}{Q}_{k,\mathrm{I}}(l)e^{ilx\tan\theta}e^{ilz}dl$$

$$+ (\tan\alpha + \tan\theta) \int_0^{+\infty} il\, \overset{\swarrow}{Q}_{k,\mathrm{I}}(l)e^{-ilx\tan\theta}e^{ilz}dl \Bigg\}.$$

$$0 = \sum_{k=1}^{\infty} \left\{ (\tan\alpha + \tan\theta) \int_0^{+\infty} (-il)\, \overset{\nearrow}{Q}_{k,\mathrm{I}}(-l) e^{ilx(\tan\alpha+\tan\theta)} e^{-ilh\tan\alpha}\, dl \right.$$

$$\left. - (\tan\alpha - \tan\theta) \int_0^{+\infty} il\, \overset{\nwarrow}{Q}_{k,\mathrm{I}}(-l) e^{ilx(\tan\alpha-\tan\theta)} e^{-ilh\tan\alpha}\, dl \right\},$$

Now, consider the second equality. Making change of variable $l \mapsto \gamma l$, with $\gamma = (\tan\alpha - \tan\theta)/(\tan\alpha + \tan\theta)$, in the first integral one obtains

$$(\tan\alpha - \tan\theta) \sum_{k=1}^{\infty} \int_0^{+\infty} il\, e^{ilx(\tan\alpha-\tan\theta)} \{ \gamma\, \overset{\nearrow}{Q}_{k,\mathrm{I}}(-\gamma l) e^{-i\gamma lh\tan\alpha} + \overset{\nwarrow}{Q}_{k,\mathrm{I}}(-l) e^{-ilh\tan\alpha} \}\, dl = 0,$$

leading to the focusing relation

$$\overset{\nwarrow}{Q}_{k,\mathrm{I}}(-l) = -\gamma\, \overset{\nearrow}{Q}_{k,\mathrm{I}}(-\gamma l) e^{ilh\tan\alpha(1-\gamma)}, \quad k = 1, 2, \ldots. \tag{17}$$

Using formulas Eqs. (16) and (15), it can be easily shown that

$$\overset{\nwarrow}{Q}_{k,\mathrm{I}}(l) = \gamma^{k-1}\vartheta_{k-2}(l)\, \overset{\searrow}{Q}_{1,\mathrm{I}}(\gamma^{k-1}l), \quad \overset{\nearrow}{Q}_{k,\mathrm{I}}(-l) = -\gamma^{k-1}\vartheta_{k-2}(l)\, \overset{\searrow}{Q}_{1,\mathrm{I}}(\gamma^{k-1}l), \tag{18}$$

$$\overset{\swarrow}{Q}_{k,\mathrm{I}}(l) = -\gamma^{k}\vartheta_{k-1}(l)\, \overset{\searrow}{Q}_{1,\mathrm{I}}(\gamma^{k}l), \quad \overset{\nwarrow}{Q}_{k,\mathrm{I}}(-l) = \gamma^{k}\vartheta_{k-1}(l)\, \overset{\searrow}{Q}_{1,\mathrm{I}}(\gamma^{k}l) e^{2ilH} \tag{19}$$

for $k = 2, 3, \ldots$, where

$$\vartheta_k(l) = \exp\left(il(h\tan\alpha(1-\gamma) - 2H) \sum_{j=0}^{k} \gamma^j \right) \tag{20}$$

and $\overset{\searrow}{Q}_{1,\mathrm{I}}(l)$ is determined in Eq. (15). Thus, functions $\psi_{k,\mathrm{I}}^-$ can be represented as the following linear integral operators:

$$\psi_{1,\mathrm{I}}^- \langle \overset{\searrow}{Q}_{1,\mathrm{I}}(l) \rangle = \int_0^{+\infty} \overset{\searrow}{Q}_{1,\mathrm{I}}(l) e^{ilx\tan\theta}(e^{ilz} - e^{-ilz})\, dl$$

$$- \int_0^{+\infty} \gamma\, \vartheta_0(l)\, \overset{\searrow}{Q}_{1,\mathrm{I}}(\gamma l) e^{-ilx\tan\theta}(e^{ilz} - e^{-ilz}e^{2ilH})\, dl \tag{21}$$

and

$$\psi_{k,\mathrm{I}}^- \langle \overset{\searrow}{Q}_{1,\mathrm{I}}(l) \rangle = -\int_0^{+\infty} \gamma^{k}\vartheta_{k-1}(l)\, \overset{\searrow}{Q}_{1,\mathrm{I}}(\gamma^{k}l) e^{-ilx\tan\theta}(e^{ilz} - e^{-ilz}e^{2ilH})\, dl$$

$$+ \int_0^{+\infty} \gamma^{k-1}\vartheta_{k-2}(l)\, \overset{\searrow}{Q}_{1,\mathrm{I}}(\gamma^{k-1}l) e^{ilx\tan\theta}(e^{ilz} - e^{-ilz})\, dl, \tag{22}$$

where $k = 2, 3, \ldots$ and $\overset{\searrow}{Q}_{1,\mathrm{I}}(l)$ is expressed in terms of Fourier spectrum $\widehat{U}_H(l)$ of the given function $U_H(z)$. Solutions for remaining cases can be constructed in a similar way (see Appendix for details).

B. Imaginary part of stream-function complex amplitude

In the previous Sec. IV A, we explained the method of solution construction and, as an example, we examined case I. Now let us check the fulfillment of boundary conditions. Here we also consider in detail case I only. Since function ψ_{I}^- is represented as an infinite sum [see Eqs. (11), (21), and (22)], one needs to consider its partial sums. To be specific, let us assume that function $U(z)$ is linear: $U(z) = A(z - B)$ with $A = 0.0005$ and $B = H/2 = 20$. Figure 4 (first and second rows) displays real parts of functions $S_{\mathrm{I,mov}}$, $S_{\mathrm{I,top}}$, $S_{\mathrm{I,bot}}$, and $S_{\mathrm{I,inc}}$, corresponding to partial sums $\psi_{\mathrm{I},1}^- \overset{\text{def}}{=} \psi_{1,\mathrm{I}}^-$ and
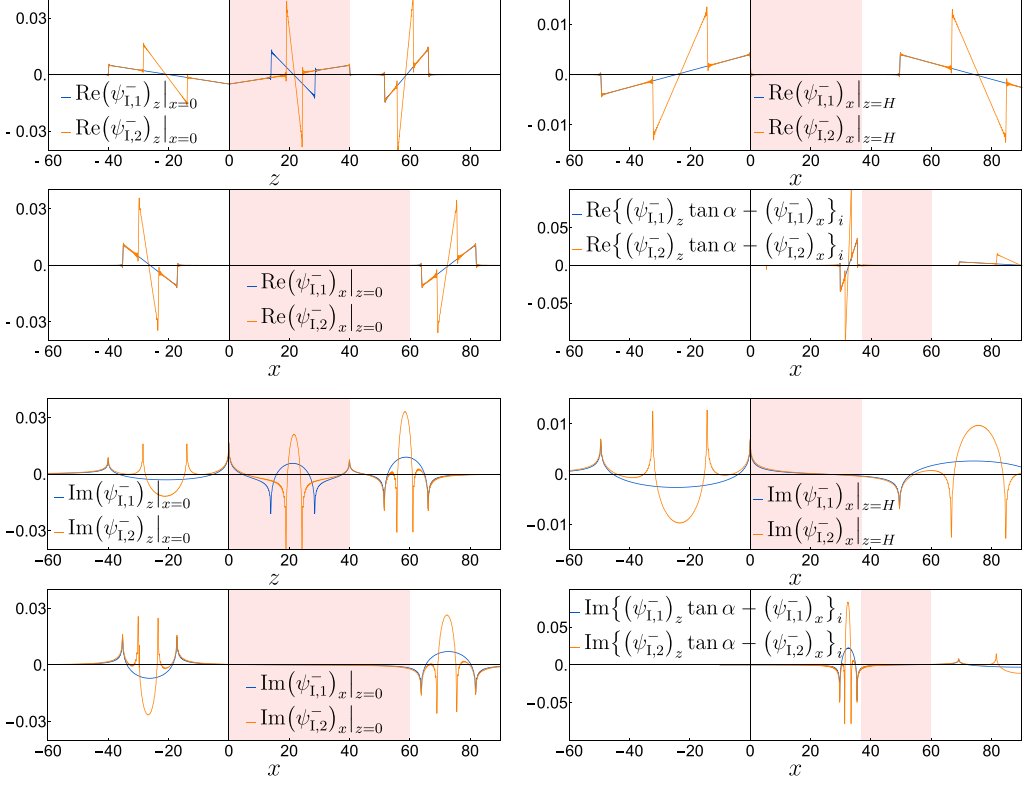
FIG. 4. Boundary conditions for partial sums $\psi_{I,1}$ and $\psi_{I,2}$ at lines $x = 0$, $x = h$, $z = 0$, and $z = \tan\alpha(h - x)$. Subscript i means that corresponding expression in the brackets is evaluated at $z = \tan\alpha(h - x)$. Pink area corresponds to each side of the trapezoid Ω. On the first and the second rows, real parts are depicted, while imaginary parts are shown in the third and the fourth rows. One can see the discrepancy at the moving wall $\Gamma = \{x = 0, z \in [0, H]\}$ (left column, first and third rows) similar to red line in Fig. 3.

$\psi_{I,2}^- \stackrel{\text{def}}{=} \psi_{1,I}^- + \psi_{2,I}^-$. One can see that inside the pink area $\text{Re } S_{I,\text{top}}$, $\text{Re } S_{I,\text{bot}}$, and $\text{Re } S_{I,\text{inc}}$ are equal to zero, meaning that corresponding boundary conditions Eqs. (7) are satisfied. The exception is provided by $\text{Re } S_{I,\text{mov}}$: there is a discrepancy with the function $U(z)$ concentrated on some interval, which becomes smaller for the second partial sum $\psi_{I,2}^-$. This phenomenon is natural, since we are dealing with a truncated series, and it will be shown in subsequent sections that the length of the discrepancy interval tends to zero with a growing amount of terms in the partial sum of the general solution. Now, let us look at Fig. 4 (third and fourth rows), where imaginary parts of functions $S_{I,\text{mov}}$, $S_{I,\text{top}}$, $S_{I,\text{bot}}$, and $S_{I,\text{inc}}$, corresponding to partial sums $\psi_{I,1}^-$ and $\psi_{I,2}^-$, are depicted. It is readily seen, that all functions inside pink area are not equal to zero, thus, boundary conditions Eqs. (7) are not satisfied and imaginary part of ψ_I^- is not a solution to the problems Eqs. (5) and (7). This can be explained by the following reasoning. For the function $U(z)$, one has

$$U_H(z) = \{I^-(z) + I^+(z)\} + i\{J^-(z) + J^+(z)\}, \tag{23}$$

where

$$I^-(z) = \frac{1}{2\pi} \text{Re} \int_0^{+\infty} \widehat{U}_H(l)e^{ilz}dl, \quad I^+(z) = \frac{1}{2\pi} \text{Re} \int_0^{+\infty} \widehat{U}_H(-l)e^{-ilz}dl, \tag{24}$$

$$J^-(z) = \frac{1}{2\pi} \text{Im} \int_0^{+\infty} \widehat{U}_H(l)e^{ilz}dl, \quad J^+(z) = \frac{1}{2\pi} \text{Im} \int_0^{+\infty} \widehat{U}_H(-l)e^{-ilz}dl. \tag{25}$$
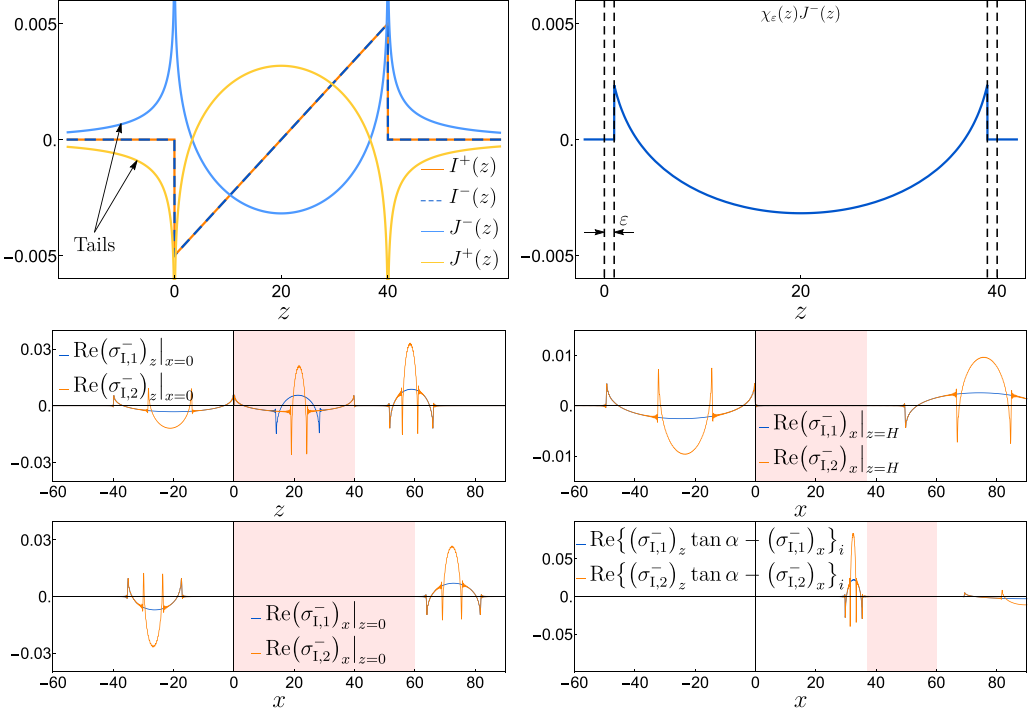
FIG. 5. First row: Left picture integrals $I^\pm$ and $J^\pm$ defined in Eq. (24) are shown; in the right picture regularization of J^- is depicted. In the second and third rows, boundary conditions for regularized partial sums of complex amplitude's imaginary parts $\eta_{I,1}$ and $\eta_{I,2}$ are shown. Subscript i means that corresponding expression in the brackets is evaluated at $z = \tan\alpha(h-x)$. Functions $\eta_{I,1}$ and $\eta_{I,2}$ are calculated for $\varepsilon = 0.1$.

Since $U_H(z)$ is a real-valued function, then (see Fig. 4)

$$I^-(z) = I^+(z), \quad J^-(z) = -J^+(z).$$

Real part of the solution ψ_I^- is generated by localized profile $I^-(z)$ [see Eq. (12)]. However, the corresponding profile for imaginary part $J^-(z)$ is nonlocalized as one can see in Fig. 5 (left picture in the fist row). Therefore, parasitic wave beams, which correspond to those parts of $J^-(z)$ lying outside $[0, H]$, will invade the domain Ω, explaining why boundary conditions will not be satisfied.

It is important to note that what's written above stands for all remaining parts of the general solution, listed in Appendix. As a result, we have only the standing-wave solution $\varphi(x, z) = \text{Re}\,\psi(x, z)$, with ψ given in Eq. (10). Now, let us discuss how to get another standing-wave solution $\eta(x, z)$. Consider a separate boundary value problem:

$$\sigma_{xx} - \lambda^2\sigma_{zz} = 0, \quad \sigma_x|_{z=0} = \widetilde{S}_{\text{bot}}(x), \quad \sigma_x|_{z=H} = \widetilde{S}_{\text{top}}(x),$$

$$\sigma_z|_{x=0} = \frac{1}{2\pi}\int_0^{+\infty}\widehat{W}_\varepsilon^-(l)e^{ilz}dl + \frac{1}{2\pi}\int_0^{+\infty}\widehat{W}_\varepsilon^+(-l)e^{-ilz}dl + \widetilde{S}_{\text{mov}}(z),$$

$$\{\sigma_z\tan\alpha - \sigma_x\}|_{z=\tan\alpha(h-x)} = \widetilde{S}_{\text{inc}}(x, z)|_{z=\tan\alpha(h-x)}. \tag{26}$$

Here

$$\widehat{W}_\varepsilon^\pm(l) = 2\int_{-\infty}^{+\infty}\chi_\varepsilon(z)J^\pm(z)e^{-ilz}dz,$$

and $\chi_\varepsilon(z)$ is the characteristic function of the interval $[\varepsilon, H - \varepsilon]$ with $\varepsilon > 0$ (see right picture in the first row of Fig. 5). The function $\chi_\varepsilon(z)$ is required for regularization of singularities of functions $J^\pm(z)$. It is readily seen that the real part of the boundary condition on the moving wall in Eqs. (26) coincides with the imaginary part of the moving boundary condition from Eq. (9) if we additionally assume $\mathrm{Im}S_{\mathrm{mov}} \overset{\mathrm{def}}{=} \mathrm{Re}\widetilde{S}_{\mathrm{mov}}$.

As in the previous subsection, the solution for case I is sought in the following form:

$$\sigma_{\mathrm{I}}^- = \sum_{k=1}^\infty \sigma_{k,\mathrm{I}}^-, \quad \sigma_{k,\mathrm{I}}^-(x,z) = \int_0^{+\infty} e^{ilx\tan\theta}\{\overset{\searrow}{R}_{k,\mathrm{I}}(l)e^{ilz} + \overset{\nearrow}{R}_{k,\mathrm{I}}(-l)e^{-ilz}\}dl$$

$$+ \int_0^{+\infty} e^{-ilx\tan\theta}\{\overset{\swarrow}{R}_{k,\mathrm{I}}(l)e^{ilz} + \overset{\nwarrow}{R}_{k,\mathrm{I}}(-l)e^{-ilz}\}dl. \tag{27}$$

The function σ_{I}^- must satisfy boundary conditions [see Eqs. (26)]:

$$(\sigma_{\mathrm{I}}^-)_z|_{x=0} = \frac{1}{2\pi}\int_0^{+\infty} \widehat{W}_\varepsilon^-(l)e^{ilz}dl + \widetilde{S}_{\mathrm{I,mov}}(z), \quad (\sigma_{\mathrm{I}}^-)_x|_{z=0} = \widetilde{S}_{\mathrm{I,bot}}(x), \tag{28}$$

$$(\sigma_{\mathrm{I}}^-)_x|_{z=H} = \widetilde{S}_{\mathrm{I,top}}(x), \quad \{(\sigma_{\mathrm{I}}^-)_z\tan\alpha - (\sigma_{\mathrm{I}}^-)_x\}|_{z=\tan\alpha(h-x)} = \widetilde{S}_{\mathrm{I,inc}}(x,z)|_{z=\tan\alpha(h-x)}. \tag{29}$$

Therefore, we arrive at the following expressions:

$$\sigma_{1,\mathrm{I}}^-\langle\overset{\searrow}{R}_{1,\mathrm{I}}(l)\rangle = \int_0^{+\infty} \overset{\searrow}{R}_{1,\mathrm{I}}(l)e^{ilx\tan\theta}(e^{ilz} - e^{-ilz})dl$$

$$- \int_0^{+\infty} \gamma\,\vartheta_0(l)\,\overset{\searrow}{R}_{1,\mathrm{I}}(\gamma l)e^{-ilx\tan\theta}(e^{ilz} - e^{-ilz}e^{2ilH})dl \tag{30}$$

and

$$\sigma_{k,\mathrm{I}}^-\langle\overset{\searrow}{R}_{1,\mathrm{I}}(l)\rangle = -\int_0^{+\infty} \gamma^k\vartheta_{k-1}(l)\,\overset{\searrow}{R}_{1,\mathrm{I}}(\gamma^k l)e^{-ilx\tan\theta}(e^{ilz} - e^{-ilz}e^{2ilH})dl$$

$$+ \int_0^{+\infty} \gamma^{k-1}\vartheta_{k-2}(l)\,\overset{\searrow}{R}_{1,\mathrm{I}}(\gamma^{k-1}l)e^{ilx\tan\theta}(e^{ilz} - e^{-ilz})dl, \tag{31}$$

where $k = 2, 3, \ldots$ and spectrum $\overset{\searrow}{R}_{1,\mathrm{I}}$ is expressed in terms of $\widehat{W}_\varepsilon^-$ as $\overset{\searrow}{R}_{1,\mathrm{I}}(l) = \widehat{W}_\varepsilon^-(l)/(2i\pi l)$. Solutions for the remaining cases can be constructed in a similar way. As a result, we constructed the second standing-wave solution as $\eta(x, z; \varepsilon) = \mathrm{Re}\,\sigma(x, z; \varepsilon)$, which is confirmed by pictures in the second and third rows of Fig. 5. Therefore, the true complex amplitude is given by the formula

$$\widetilde{\psi}(x, z; \varepsilon) = \varphi(x, z) + i\eta(x, z; \varepsilon). \tag{32}$$

It is necessary to note that function η is the solution for every ε. Moreover, the solution η is not unique, because one can consider any function $J^-(z)$ with support lying inside the interval $[0, H]$. When the internal wave-generation problem is considered in an infinite domain, one must take into account so-called radiation conditions, meaning that energy should propagate away from the source [49,50]. These conditions give additional constraint, relating real and imaginary parts of the complex amplitude and, therefore, allowing us to select a unique solution. However, in a confined domain

it is not clear how to impose such a condition properly [51], hence, the nonuniqueness problem remains unresolved.

V. PARTIAL SUMS OF THE GENERAL SOLUTION

As discussed in the previous section, one should consider partial sums of the solution constructed. We define a partial sums of series corresponding to each case I–VI in special form

$$\psi_{I,K}^- = \sum_{j=1}^{K} \psi_{j,I}^- \langle \overset{\searrow}{Q}_{1,I}(l) \rangle, \quad \psi_{II,K}^+ = \psi_{1,II}^+ \langle \overset{\nearrow}{Q}_{1,II}(-l) \rangle + \sum_{j=2}^{K} \psi_{j,K,II}^+ \langle \overset{\nearrow}{Q}_{1,II}(-l) \rangle,$$

$$\psi_{III,K}^+ = \sum_{j=1}^{K} \psi_{j,III}^+ \langle \overset{\nearrow}{Q}_{1,III}(-l) \rangle, \quad \psi_{IV,K}^+ = \sum_{j=1}^{K} \psi_{j,IV}^+ \langle \overset{\nearrow}{Q}_{1,IV}(-l) \rangle,$$

$$\psi_{V,K}^+ = \sum_{j=1}^{K} \psi_{j,V}^+ \langle \overset{\nearrow}{Q}_{1,V}(-l) \rangle, \quad \psi_{VI,K}^+ = \sum_{j=1}^{K} \psi_{j,VI}^+ \langle \overset{\nearrow}{Q}_{1,VI}(-l) \rangle, \tag{33}$$

where each term $\psi_{j,K,II}^+$ is of the form

$$\psi_{j,K,II}^+ = \int_0^{+\infty} \frac{e^{-ilH}}{4i\pi^2 l} (\widehat{U}_{j-1} * \widehat{\chi}_3)(-l)(e^{il(z-H)} - e^{-il(z-H)})e^{ilx\tan\theta} dl$$

$$- \int_0^{+\infty} \varkappa(l) \frac{e^{-il\gamma^{-1}H}}{4i\pi^2 l} (\widehat{U}_{j-1} * \widehat{\chi}_3)(-\gamma^{-1}l)(e^{il(z-H)} - e^{-il(z-H)}e^{-2ilH})e^{-ilx\tan\theta} dl$$

$$- \psi_{III,K-j+1}^+ \left\langle \frac{1}{4i\pi^2 l}(\widehat{U}_{j-1} * \widehat{\chi}_1)(-l) \right\rangle - \psi_{IV,K-j+1}^+ \left\langle \frac{e^{-ilH}}{4i\pi^2 l}(\widehat{U}_{j-1} * \widehat{\chi}_2)(-l) \right\rangle$$

$$- \psi_{V,K-j+1}^+ \left\langle \frac{e^{-ilH}}{4i\pi^2 l}(\widehat{U}_{j-1} * \widehat{\chi}_4)(-l) \right\rangle - \psi_{VI,K-j+1}^+ \left\langle \frac{e^{-ilH}}{4i\pi^2 l}(\widehat{U}_{j-1} * \widehat{\chi}_5)(-l) \right\rangle, \tag{34}$$

for $j = 2, 3, \ldots$ and $\widehat{U}_{j-1}$ defined in (A19). The above formulas have clear physical meaning: such partial sums correspond to wave-beam solutions passing full cycle inside the domain Ω (i.e., starting from the left boundary and ending up at the same boundary) K times. Partial sums $\sigma_K(x, z; \varepsilon)$ are defined in a similar way. Thus, in further sections we are going to deal with the solution

$$\varphi_K(x, z) = \Phi_K + \text{Re}\{\psi_{I,K}^- + \psi_{II,K}^+ + \psi_{III,K}^+ + \psi_{IV,K}^+ + \psi_{V,K}^+ + \psi_{VI,K}^+\},$$

$$\eta_K(x, z; \varepsilon) = \Theta_K + \text{Re}\{\sigma_{I,K}^- + \sigma_{II,K}^+ + \sigma_{III,K}^+ + \sigma_{IV,K}^+ + \sigma_{V,K}^+ + \sigma_{VI,K}^+\},$$

where Φ_K and Θ_K are real-valued arbitrary constants, which will be defined further in such a way that $\varphi_K|_{\partial\Omega/\Gamma} = \eta_K|_{\partial\Omega/\Gamma} = 0$ (remember here that $\Gamma = \{x = 0, z \in [0, H]\}$). Therefore, the complex amplitude of the stream function is given by the limit

$$\widetilde{\psi}(x, z; \varepsilon) = \varphi(x, z) + i\eta(x, z; \varepsilon) = \lim_{K \to +\infty} \{\varphi_K(x, z) + i\eta_K(x, z; \varepsilon)\}.$$

VI. NUMERICAL TESTS

For numerical tests, we take the following set of parameters: the dimensionless height $H = 40$, length $h = 60$, inclination angle $\alpha = \pi/3$, and frequency $\omega = \pi/5$ (corresponding to propagation angle $\theta = \arcsin \pi/5$). The forcing is taken as above: $U(z) = A(z - B)$, where $A = 2\omega a/H$ with $a = 0.01$ and $B = H/2$. We use WOLFRAM MATHEMATICA for computations of all Fourier integrals by the standard approximation *NIntegrate* with the integration interval bounded by upper limit $l = 60$ for the stream function and $l = 110$ for velocity components. In addition, we performed
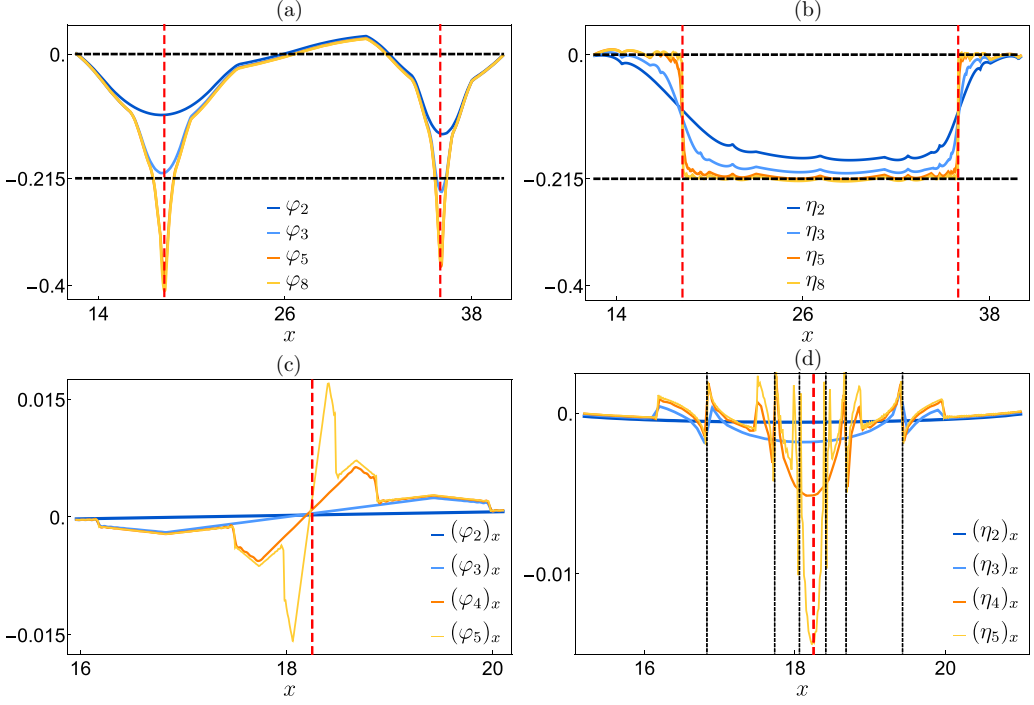
FIG. 6. (a), (b) Cross-sectional profiles of stream function's real φ_K and imaginary η_K parts for $K = 2, 3, 5, 8$ are shown correspondingly. Dashed lines traced at 0 and -0.215 as a guide to the eye. (c), (d) Cross-sectional profiles of vertical velocity component's real $(\varphi_K)_x$ and imaginary $(\eta_K)_x$ parts for $K = 2, 3, 4, 5$ are shown, respectively. Functions η_K are calculated for $\varepsilon = 0.1$.

direct numerical simulations (DNSs) for low-viscosity cases, which are discussed below in more detail.

A. Convergence test

Prior to comparison of our solution with the one obtained by DNS, we evaluate the number of beam cycles sufficient to approximate the exact analytical solution by truncated series. To do this, we take partial sums φ_K and η_K with $K = 2, 3, 5, 8$, evaluated at the cross section $z = \cot\theta(x - 36) + 29.1$ orthogonal to attractor arms (see Fig. 8, red line in the left picture). The results are shown in Figs. 6(a) and 6(b). One can observe pointwise convergence: the difference between subsequent partial sums decreases everywhere except for two singularity points corresponding to vertical red dashed lines. For each $K = 2, 3, 5, 8$, constants Φ_K and Θ_K are chosen as follows:

$$\Phi_2 = 0.0129, \quad \Phi_3 = 0.0156, \quad \Phi_5 = 0.0171, \quad \Phi_8 = 0.0173,$$

$$\Theta_2 = 0.1703, \quad \Theta_3 = 0.1909, \quad \Theta_5 = 0.2018, \quad \Theta_8 = 0.2045.$$

Also, one can see that partial sums φ_5 and η_5 are rather good approximations of solutions φ and η.

Vertical velocity component profiles for $K = 2, 3, 4, 5$ evaluated at cross section $z = \cot\theta(x - 36) + 29.1$ for $12 \leqslant x \leqslant 25$ are shown in Figs. 6(c) and 6(d). It is clearly seen that as K increases the velocity amplitude grows in the vicinity of the attractor arm (vertical red dashed lines). Also, there are multiple spikes in the $(\eta_K)_x$ profile, which are denoted by vertical black dashed lines. These spikes result from regularization of singularities at the moving boundary (see Fig. 5, first row, right picture). Thus, decreasing parameter ε should result in more pronounced spikes [see Fig. 7(a)].
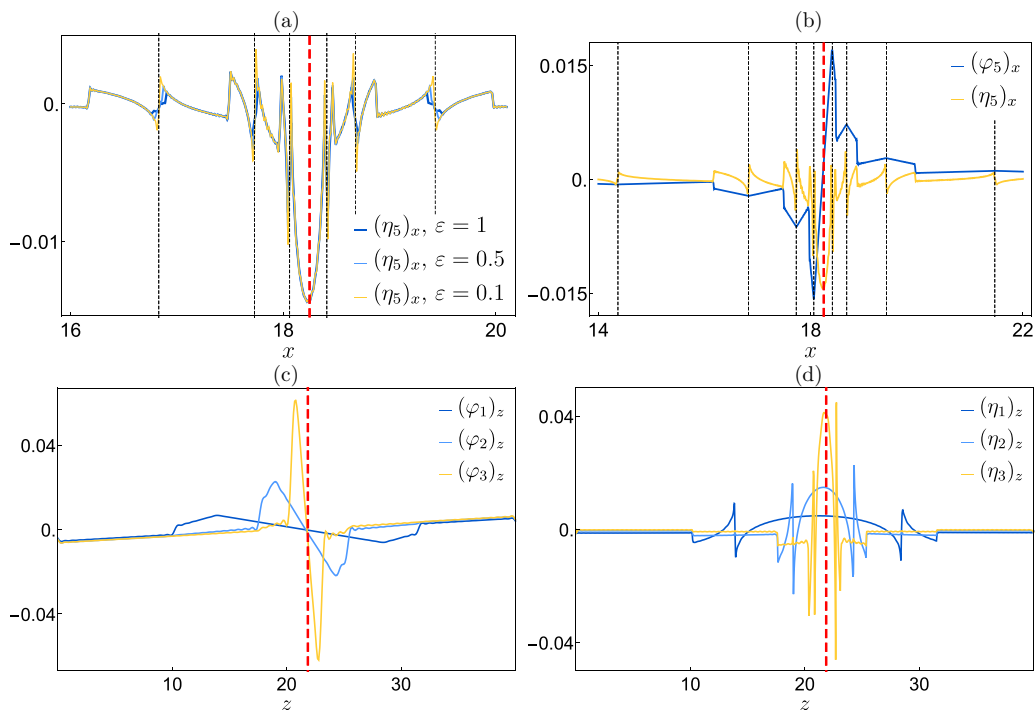
FIG. 7. (a) Variation of the parameter $\varepsilon = 1; 0.5; 0.1$ in $(\eta_5)_x$ leading to more pronounced spikes. (b) Vertical velocity component profiles $(\varphi_5)_x$ and $(\eta_5)_x$, evaluated at cross section $z = \cot\theta(x - 36) + 29.1$ for $12 \leqslant x \leqslant 25$. (c), (d) Profiles of $(\varphi_K)_z$ and $(\eta_K)_z$ evaluated at $x = 0$ for $K = 1, 2, 3$.

It is necessary to note that, by construction, partial sums φ_K and η_K satisfy boundary conditions everywhere except the moving wall. However, the domain in the neighborhood of the left reflection point of the wave-ray attractor, within which the boundary condition is not satisfied, shrinks with growing K [see Figs. 7(c) and 7(d)].

B. Comparison with direct numerical simulations

Since in laboratory experiments, fluid is viscous and salt-stratified, then one should take into account salt diffusion in the mass conservation equation. Let us note in passing that we restrict our attention to the case where the mass diffusivity is low compared to kinematic viscosity. We consider the case of weak stratification, allowing us to use the Boussinesq approximation, i.e., system of equations to be solved numerically is of the following form:

$$\mathbf{u}_t + (\mathbf{u} \cdot \nabla)\mathbf{u} = -\frac{1}{\rho_*}\nabla p + \nu\Delta\mathbf{u} + \mathbf{g}\frac{\rho'}{\rho_*},$$

$$\rho'_t + (\mathbf{u} \cdot \nabla)\rho' = \lambda\Delta\rho' - v\frac{d\rho_0}{dz}, \quad \nabla \cdot \mathbf{u} = 0,$$

where ν is kinematic viscosity coefficient, $\mathbf{u} = (u, v)$ is velocity field, p is pressure fluctuation with respect to hydrostatic equilibrium $dp_0/dz = -g(\rho_* + \rho_0(z))$, $\rho_* = 1$ [g/cm^3] is characteristic density, $\rho_0(z)$ is linear density profile at rest with the gradient $d\rho_0/dz \approx -0.00101937$ [g/cm^4], ρ' is density fluctuation, and λ is salt diffusion coefficient. We specify no-slip boundary conditions at all rigid surfaces except for the vertical wall, where the profile of the horizontal velocity is prescribed: $u(0, z, t) = U(z)\sin\omega t$. Also, we specify the normal derivative of ρ' at a rigid boundary to be
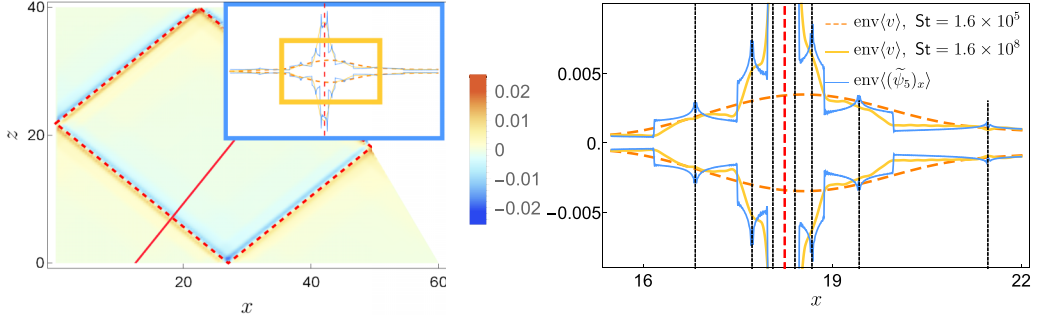
FIG. 8. Left: Snapshot of vertical velocity field v, obtained by DNS (underlying picture). Comparison of numerical simulations for different values of Stokes number St with approximate solution $(\widetilde{\psi}_x)_5$ at the cross section $z = \cot\theta(x - 36) + 29.1$ for $12 \leqslant x \leqslant 25$ (red line) is shown in the light blue box. Right: Picture zoomed-in yellow box is shown. Dashed orange and yellow curves are envelopes of vertical velocity profiles, obtained by numerical simulation with $\nu = 10^{-2}$ and $\nu = 10^{-5}$, correspondingly. Light blue curves are envelopes of vertical velocity profile corresponding to the approximate solution $(\widetilde{\psi}_5)_x$.

zero and at $t = 0$ the fluid is in rest. The DNSs are performed using semi-implicit third-order time integration scheme and spatial discretisation based on the spectral-element method, implemented in open source computational fluid dynamics solver Nek5000 (see Refs. [52,53]). To compare our approximate inviscid velocity field with that calculated numerically we choose the kinematic viscosity coefficient $\nu = 10^{-2}$; 10^{-3}; 10^{-4}, and 10^{-5} [cm^2/s], covering three orders of magnitude below the viscosity of the tap water, and corresponding to the values of the global Stokes number St $= H^2 N/\nu = 1.6 \times 10^5$; 1.6×10^6; 1.6×10^7, and 1.6×10^8. In all DNSs presented below, the value of the Schmidt number is kept constant so Sc $= \nu/\lambda = 100$. In preliminary simulations we used Sc between 10 and 700. Since the results were found to be very weakly sensitive to the actual value of Sc provided $1 \ll$ Sc we selected Sc $= 100$ as a representative value for a salt-stratified case (disregarding a specific type of salt). The geometry of the setup and the nondimensional frequency were taken precisely the same as in the beginning of Sec. VI.

To perform the comparison we calculate vertical velocity field with linear profile $U(z)$ at moving boundary (see beginning of Sec VI) at instants $t_1 \approx 200T_0$ and $t_2 = t_1 + T_0/4$, with T_0 being the forcing period. These instants correspond to real and imaginary parts of complex amplitude $\widetilde{\psi}$. Then we consider the wave field at the cross section specified by equation $z - \cot\theta(x - 36) + 29.1 = 0$ depicted by the solid red line in the left panel of Fig. 8. In the right panel of Fig. 8, we present the comparison between the envelope,

$$\text{env}\langle v \rangle = \pm\sqrt{v^2 + (v^s)^2}, \quad v = v(x, z, t_1), \quad v^s = v(x, z, t_2), \tag{35}$$

of the vertical velocity component v calculated in DNSs at St $= 1.6 \times 10^5$ and St $= 1.6 \times 10^8$ and the envelope of $(\widetilde{\psi}_5)_x$,

$$\text{env}\langle(\widetilde{\psi}_5)_x\rangle = \pm\sqrt{(\varphi_5)_x^2 + (\eta_5)_x^2}, \tag{36}$$

evaluated at the same cross section. To compare the curves in detail we present the profiles of these envelopes for $12 \leqslant x \leqslant 25$. The same data covering a larger range of x are shown at the inset (blue rectangle) in the left panel of Fig. 8.

Now, let us discuss the physically important effects of the finite value of the Stokes number in light of the structure of the inviscid solution. First, we note that the envelope profile obtained in DNSs at St $= 1.6 \times 10^8$ (solid yellow line) has the structure of nested boundary layers, which is in excellent qualitative agreement with the nested structure of the inviscid solution (solid blue line), the former being a smoothed regularized version of the latter. Moreover, as could be anticipated,

the larger the spatial scale of the profile features, the better the quantitative agreement between the inviscid solution and the numerical solution obtained at low viscosity (St $= 1.6 \times 10^8$). Thus, the inviscid solution describes well the background wave motion in the bulk of the fluid, with the exception of (i) the boundary layers at the rigid walls and (ii) the fine-scaled nested boundary layers in the close vicinity of the ray skeleton of the attractor (depicted by vertical dash red line in Fig. 8). Note that the background wave motion has small but nonzero amplitudes that may be of importance for future consideration of weakly nonlinear problems since secondary waves emitted from the primary wave beams due to triadic resonance instability may interfere with the background motion.

Second, we note that the envelope profile obtained in DNSs at St $= 1.6 \times 10^5$ (orange dash line) has a bell-shaped form reminding us of the Gaussian envelope for a self-similar solution [14]. However, it can be clearly seen that the right and left tails of the envelope are nonsymmetrical and do not tend to zero in the way expected for a Gaussian curve. Moreover, the maximum of the envelope calculated for St $= 1.6 \times 10^5$ (orange dash line) is displaced from the location of the ray skeleton of the wave attractor (vertical red dash line in Fig. 8). This is a consequence of the nonsymmetrical shape of the envelope of the inviscid solution seen in the right panel of Fig. 8 (solid light blue line). Note that these features appear in the experimental data obtained at St of order 10^5 [18]. Summing up, both at St $= 1.6 \times 10^8$ and at St $= 1.6 \times 10^5$, we can identify relevant observable features of the wave envelope profiles which can be traced back to the structure of the inviscid solution. In future research, we are planning to consider a viscous regularization of the inviscid solution.

As mentioned in the Introduction, in unbounded domains one can relate the prescribed form of motion of the wave generator with the motion in the radiated internal wave beam [25]. In a confined domain in the presence of wave focusing and defocusing, such relation is much less straightforward, as shown in previous sections of this paper. Below, we compare explicitly the forms of wave motion in the wave attractor induced by two wave generators. The first wave generator consists of the linear profile $U(z)$ given in the beginning of Sec. VI and corresponding complex amplitude and velocity components are denoted by index l. The second wave generator profile is a half wavelength of the cosine with the same amplitude: $U_c(z) = -0.01 \cos (\pi z/40)$. In this case, corresponding complex amplitude and velocity components are denoted by index c. Again, we consider the wave field at the cross section $z - \cot \theta (x - 36) + 29.1 = 0$.

The result of comparison is shown in Fig. 9, where the vertical velocity envelopes and the instantaneous vertical velocity profiles are presented in the left and right columns, respectively, while the rows (from upper to lower) show the approximate inviscid solution and the results of DNSs at St $= 10^8$ and St $= 10^5$. Note that the results of calculations for the wavemaker whose shape is prescribed as a half wavelength of the cosine function $U_c(z)$ are multiplied by the quantity $\kappa = 8/\pi^2$. After this normalization, the results for both wavemakers have comparable amplitudes. In the inviscid case, one can easily identify the effect of the shape of the wave generator. This is particularly well seen in the instantaneous vertical velocity profiles: the real part in the two cases under consideration represents a piecewise combination of either straight lines or cosine arcs. However, an experimental observation of this effect may be problematic. One may need to perform experiments at a very high value of the Stokes number, which cannot be obtained in practice. Otherwise, the effect of the wave-generator shape on the form of wave motion is hidden by viscosity. Indeed, the results of DNSs (see panels of Fig. 9) appear to be almost undistinguishable, both in terms of wave envelopes and in terms of instantaneous velocity profiles. Given the typical errors of particle image velocimetry or synthetic Schlieren techniques, the difference between the profiles would be hard to identify. The only easily measurable quantity is κ, i.e., the ratio of the wave amplitudes in the two cases under consideration. The origin of this coefficient is straightforward: it stands as the common multiplier in the Fourier series for the even triangular wave.

Although we considered only two profiles of wave generators, we can make a plausible conjecture that the efficiency of any particular volume-conserving generator is proportional to the amplitude of the first term in the expansion of the generator shape into the Fourier series. In that sense, the generators used in Ref. [19] have maximum efficiency in terms of exciting the highest
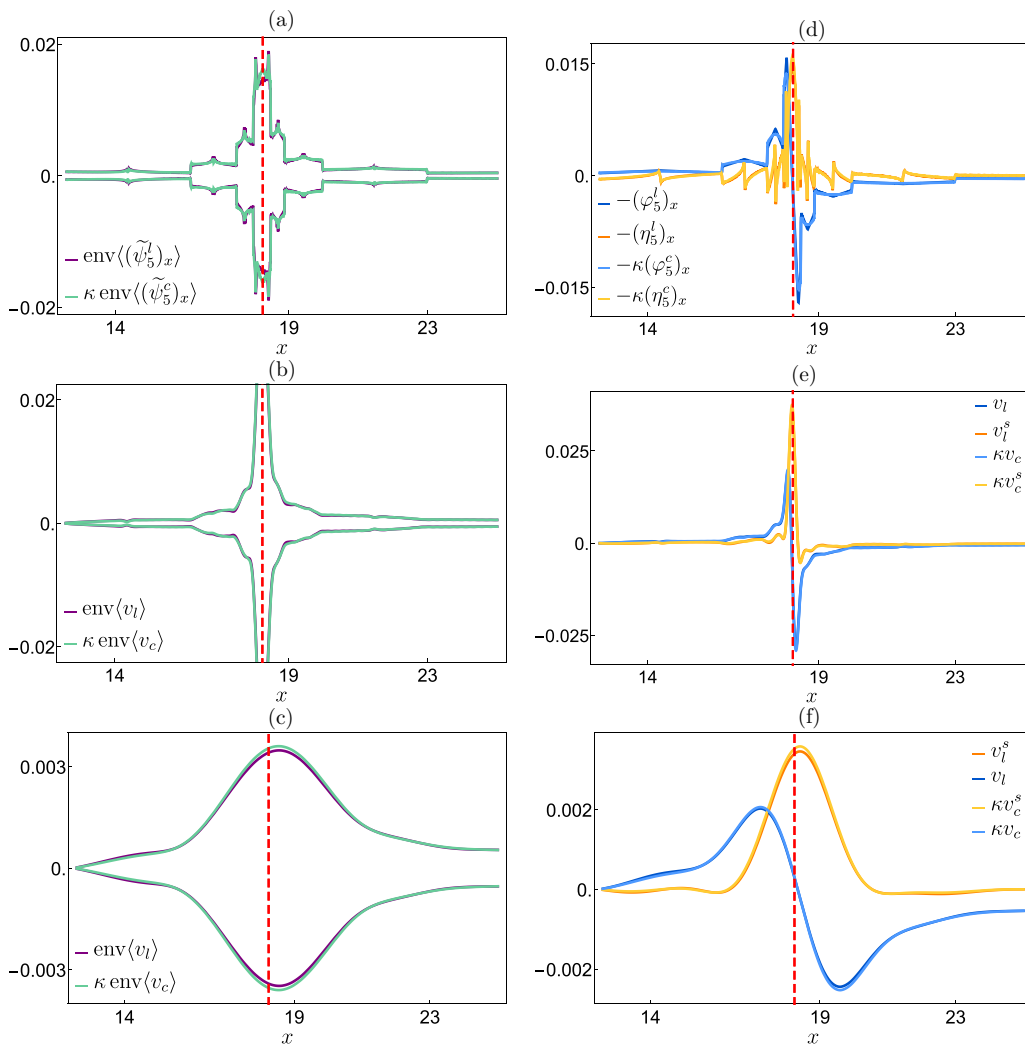
FIG. 9. Comparison of the solutions for linear and cosine wave generators. Left column: Vertical velocity envelopes. Right column: Instantaneous vertical velocity profiles. Rows (top to bottom): Approximate inviscid solution, DNS for $St = 10^8$ and $St = 10^5$.

possible wave amplitude at a given amplitude of the wave maker. On the other hand, the technical simplicity of the wave generator with linear profile, which is a pivoting flat plate undergoing torsional oscillations around a horizontal axis fixed at half depth of the liquid volume, may be appealing in applications. A slightly lower efficiency of wave generation (by factor κ as compared to the wave generator with cosine profile) can easily be compensated by setting a higher oscillation amplitude.

Finally, let us make an observation concerning the duration of the transient regime required to reach the saturated steady-state wave regime in the attractor. The DNSs were performed by switching on the prescribed forcing in an initially quiescent fluid. The duration of the transient regime can be conveniently quantified by plotting the total kinetic energy of the system as a function of time. As could be expected, the duration of the transient regime and the saturated value of the total kinetic energy tremendously increases with the Stokes number.
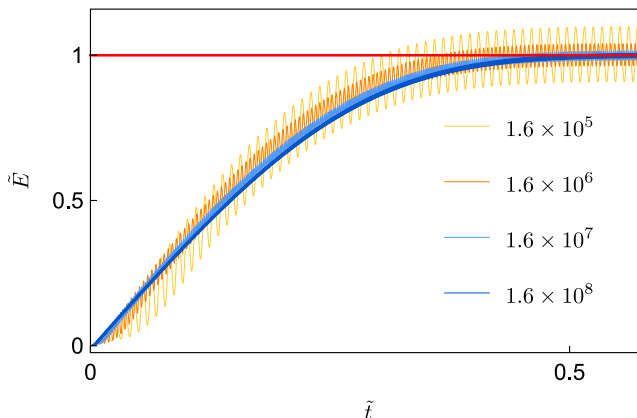
FIG. 10. Comparison of the normalized total kinetic energy $\tilde{E}$ against normalized time $\tilde{t}$ for different Stokes numbers St $= 1.6 \times 10^5$, 1.6×10^6, 1.6×10^7, 1.6×10^8, where $\tilde{E} = E/E_{\mathrm{mean}}$, with E_{mean} being the averaged kinetic energy over one period T_0 at $t \longrightarrow \infty$, and $\tilde{t} = t/(T_0 \mathrm{St}^{1/3})$.

However, by introducing appropriate scaling, the energy time-history curves obtained at different values of the Stokes number collapse onto a nearly universal curve. Let us introduce the normalized kinetic energy as $\tilde{E} = E(t)/E_{\mathrm{mean}}$, where E_{mean} denotes the kinetic energy averaged over the forcing period T_0, with the averaging performed in the saturated regime of steady-state oscillations reached at $t > t_*$. Further, using the viscous timescale σ_b^2/ν, where the beam width σ_b scales as $(\sigma_b/H) \sim \mathrm{St}^{-1/3}$, we can introduce the nondimensional time as $\tilde{t} = t/(T_0 \mathrm{St}^{1/3})$. The results of numerical calculations performed at St $= 1.6 \times 10^5$, 1.6×10^6, 1.6×10^7, and 1.6×10^8 are presented in Fig. 10. It can be seen that the obtained curves exhibit similar behaviors at sufficiently large time, and the duration of transients in the system in the considered range of parameters can be taken as $\tilde{t}_* = 0.5$. In the case of rotating fluid, a similar estimate applies, with the Stokes number St replaced by inverse Ekman number Ek^{-1} and different nondimensional values of $\tilde{t}_*$. For typical conditions of experiments with an internal wave attractor [18], we have St of the order of about 10^5, yielding the transient time equal to about 20 forcing periods, which is in a good agreement with observations. Note that extrapolation of this scaling to large-scale objects yields very large estimates. Consider a thought experiment with the same geometric setup and frequency $\omega/N = \pi/10$, upscaled to depth $H = 4000$ m, with $N = 10^{-3}$ s^{-1} and $\nu = 10^{-6}$ m^2/s. In this case, the transient time t_* is about 1260 forcing periods or 145 days. For oceanic systems, one usually has lower values of ω/N and a horizontally elongated geometry with much higher h/H. If the viscous timescale remains relevant for elongated geometry, corresponding estimates can be performed by using formula (4.5) in Ref. [20] and assuming universal $\tilde{t}_* = 0.5$. Clearly, the transient time (even with, say, three orders of magnitude higher eddy viscosity, replacing molecular viscosity) appears to be comparable with the time of seasonal variations of the background stratification $N(z, t)$ in natural systems. This puts into perspective the duration of transients in numerical simulations of natural systems [54] and suggests that, under natural conditions, wave attractors might arise and disappear in sporadic fashion when appropriate ray geometry is reached (in spirit of Ref. [55]) for slowly evolving $N(z, t)$, so the fully saturated regime is never reached.

VII. CONCLUSIONS AND DISCUSSION

This paper is focused on construction of an analytical solution for the problem of internal-wave motion in a confined trapezoidal domain filled with an ideal uniformly stratified fluid. The perturbation is introduced by the moving wall which serves as the wave generator. The procedure allows us to construct a solution for volume-conserving motion of the wall, and relate the spectrum

of the boundary motion to the spectrum of the internal wave motion. Under the appropriate choice of parameters, the setup supports the internal wave attractors. The solution for the parallelogram-shaped wave attractor (having one reflection at each wall of the trapezoidal domain) is constructed as an iterative superposition of localized wave beams fulfilling the nonpermeability conditions at the rigid boundaries of the domain. Once generated at the moving wall, wave beams spread energy away from the source and, on first sight, it is in accordance with the common meaning of the radiation condition [49]. But when these wave beams reflect from boundary, the energy propagates toward the source, and it is not obvious how to impose radiation conditions properly (it was also pointed in Refs. [10,12,51] and other works). Therefore, absence of properly imposed radiation conditions and separation of the complex amplitude's real and imaginary parts result in underdeterminacy of the problem (which is one of the manifestations of its ill posedness).

It is also important to note that the constructed solution can be further used to explore weakly nonlinear perturbations of the wave beams (e.g., in the spirit of Refs. [34,36]) and to consider viscous regularization (another way of regularization can be found in Ref. [56]) of the problem by appropriate viscous damping of the spectral components of the inviscid solution.

The approximate analytical solution is compared against the results of DNSs performed with the help of the spectral element method. This comparison allowed us to identify the features of the weakly viscous numerical solution which can be interpreted in terms of the inviscid solution. The wave motion in the bulk of the fluid domain (away from the rigid boundaries and the wave-ray skeleton of the attractor) is well described by the inviscid solution, which is in a good quantitative agreement with the weakly viscous numerical solution. Physically, this could be expected since the wave motion in the bulk of fluid corresponds to low wave numbers, which are weakly damped by viscosity. The wave envelopes calculated for the Stokes number of order 10^5, the value typical for laboratory experiments, exhibit nonsymmetry with respect to the position of the wave-ray skeleton of the attractor, both in terms of the position of the maximum of the profile and the shape of "tails." This is related to the nonsymmetry of the inviscid solution. At the Stokes number of order 10^8, we observe the nested boundary layer structure in the vicinity of the wave-ray skeleton, in perfect agreement with the nested structure of the inviscid solution.

Further, we explored the role of the shape of the wave generator on the instantaneous profiles and envelopes of the wave beams. In the inviscid limit, there is a clear relation: for wave-generator shapes given by the linear function and by the cosine function, the real part of the wave profiles is a piecewise construction of linear and arc-of-cosine segments, respectively. In the weakly viscous case in the studied range of the Stokes number covering three orders of magnitude (between 1.6×10^5 and 1.6×10^8), the calculated profiles are very weakly sensitive to the particular shape of the generator. Experimentally, the difference between the profiles would be hard to detect given the current state of the art of the existing measurement techniques (particle image velocimetry and synthetic Schlieren). However, being very similar in terms of shape of the wave profiles, the two cases are easily distinguished by amplitude of the wave motions. This is related to the fact that focusing quickly decreases the relevant length scales in the vicinity of the attractor skeleton so only the largest scale spectral component of the generator shape survives. Thus, the relative efficiency of a particular profile of the wave generator is given by the first term in the Fourier series representing the shape of the profile. If the amplitude of oscillation for cosine-shaped and linear-shaped wave generators is the same, the amplitude of wave motion is $8/\pi^2$ times smaller in the latter case.

Finally, we show that the typical duration of transients in DNSs of the wave attractors is governed by the viscous tim scale. Under appropriate rescaling, the time histories of total kinetic energies of the wave attractors (where the wave motion starts from the rest) collapse onto a common curve. The estimates of the duration of transient processes are in good agreement with experiments performed at the Stokes number of the order of 10^5. Care must be taken regarding the physical relevance of extrapolation of such estimates to large physical objects at ocean-depth (or planetary) scale, where the relevant values of the Stokes number exceed the typical experimental values by several orders of magnitude.
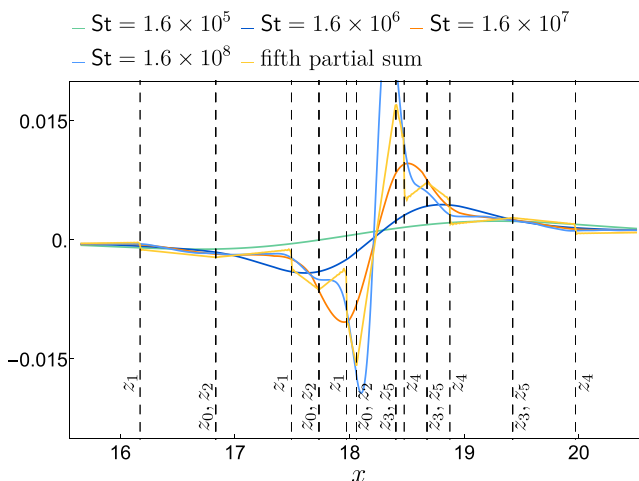
FIG. 11. The real part of the fifth partial sum of the theoretical solution $(\varphi_5)_x = \mathrm{Re} \sum_{K=1}^{5} \{\psi_{I,K}^- + \ldots + \psi_{VI,K}^+\}$ versus DNS at different values of the Stokes number. Vertical dashed lines correspond to points z_i under characteristic map.

Note that the solution consists of two types of singularities: primary (attractor itself) and secondary singularities emanating from trapezium corners. The filtering procedure described in Sec. IV B affects the positions of secondary singularities as shown in Figs. 11–13: the true solution (with filtering) traces singularities from the left corners of the trapezium (points z_0 and z_5) and discontinuities from the right corners of the trapezium (points z_1 and z_4), whereas the solution without filtering is singular at characteristics tracing points z_1, z_4 and continuous at characteristics tracing the other points. Here we might introduce a filtering procedure which could be performed in a smoother way (for instance, by taking a convolution with an appropriate mollifier). However, we believe that such a strategy is not optimal: the smoothing of boundary conditions would not
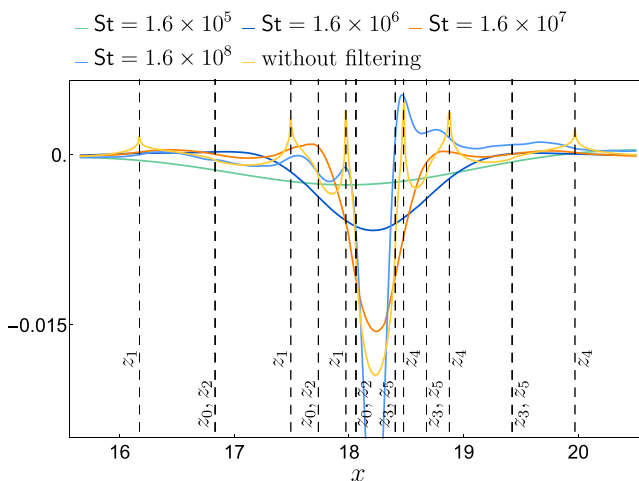

FIG. 12. The imaginary part of the fifth partial sum of the theoretical solution without filtering $\mathrm{Im} \sum_{K=1}^{5} \{\psi_{I,K}^- + \ldots + \psi_{VI,K}^+\}$ versus DNS at different values of the Stokes number. Vertical dashed lines correspond to points z_i under characteristic map.

FIG. 13. The imaginary part of fifth partial sum of the theoretical solution after filtering $(\eta_5)_x =$ Re $\sum_{K=1}^{5}\{\sigma_{I,K}^- + \ldots + \sigma_{VI,K}^+\}$ versus DNS at different values of the Stokes number. Vertical dashed lines correspond to points z_i under characteristic map.
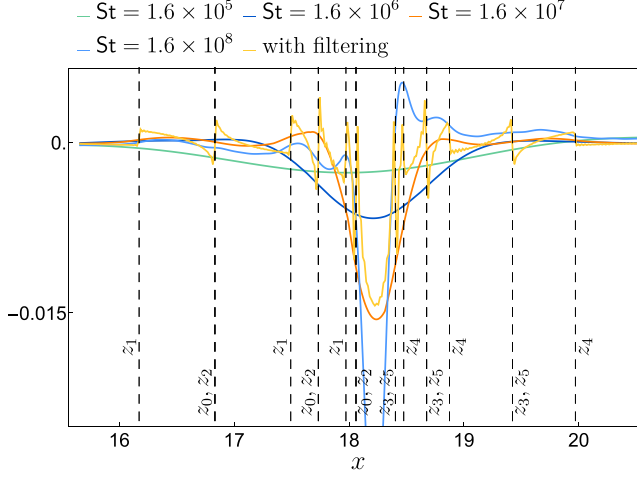
give us any new physically meaningful features. Ultimately, after adding the viscous attenuation, the nonphysical singularities and discontinuities would disappear (as shown by DNS).

ACKNOWLEDGMENTS

APPENDIX: SOLUTIONS FOR REMAINING CASES

1. Cases III and IV

Functions ψ_{III}^+ and ψ_{IV}^+ must satisfy boundary conditions

$$(\psi_{\text{III}}^+)_z|_{x=0} = \frac{1}{4\pi^2}\int_0^{+\infty}(\widehat{U} * \widehat{\chi}_1)(-l)e^{-ilz}dl + S_{\text{III,mov}}(z), \quad (\psi_{\text{III}}^+)_x|_{z=0} = S_{\text{III,bot}}(x),$$

$$(\psi_{\text{III}}^+)_x|_{z=H} = S_{\text{III,top}}(x), \quad \{(\psi_{\text{III}}^+)_z \tan\alpha - (\psi_{\text{III}}^+)_x\}|_{z=\tan\alpha(h-x)} = S_{\text{III,inc}}(x,z)|_{z=\tan\alpha(h-x)}$$

and

$$(\psi_{\text{IV}}^+)_z|_{x=0} = \frac{1}{4\pi^2}\int_0^{+\infty}(\widehat{U} * \widehat{\chi}_2)(-l)e^{-ilz}dl + S_{\text{IV,mov}}(z), \quad (\psi_{\text{IV}}^+)_x|_{z=0} = S_{\text{IV,bot}}(x),$$

$$(\psi_{\text{IV}}^+)_x|_{z=H} = S_{\text{IV,top}}(x), \quad \{(\psi_{\text{IV}}^+)_z \tan\alpha - (\psi_{\text{IV}}^+)_x\}|_{z=\tan\alpha(h-x)} = S_{\text{IV},inc}(x,z)|_{z=\tan\alpha(h-x)},$$

correspondingly, where χ_1 and χ_2 are characteristic functions of intervals $[z_0, z_1]$ and $[z_1, z_2]$. Then, solutions are

$$\psi_{\text{III}}^+ = \sum_{j=1}^{\infty} \psi_{j,\text{III}}^+ \langle \overset{\nearrow}{Q}_{1,\text{III}}(-l)\rangle, \quad \psi_{\text{IV}}^+ = \sum_{j=1}^{\infty} \psi_{j,\text{IV}}^+ \langle \overset{\nearrow}{Q}_{1,\text{IV}}(-l)\rangle,$$

$$\psi_{1,\text{III}}^+ \langle \overset{\nearrow}{Q}_{1,\text{III}}(-l)\rangle = \int_0^{+\infty} \overset{\nearrow}{Q}_{1,\text{III}}(-l) e^{ilx\tan\theta} e^{-ilz} dl$$

$$+ \int_0^{+\infty} \gamma\,\vartheta_0(l)\, \overset{\nearrow}{Q}_{1,\text{III}}(-\gamma l) e^{-ilx\tan\theta}(e^{ilz} - e^{-ilz}e^{2ilH}) dl, \qquad (A1)$$

$$\psi_{1,\text{IV}}^+ \langle \overset{\nearrow}{Q}_{1,\text{IV}}(-l)\rangle = -\int_0^{+\infty} \overset{\nearrow}{Q}_{1,\text{IV}}(-l) e^{ilx\tan\theta}(e^{il(z-H)} - e^{-il(z-H)}) dl$$

$$+ \int_0^{+\infty} \gamma^{-1}\varkappa(l)\, \overset{\nearrow}{Q}_{1,\text{IV}}(-\gamma^{-1}l) e^{-ilx\tan\theta} e^{il(z-H)} dl,$$

$$\psi_{k,\text{III}}^+ \langle \overset{\nearrow}{Q}_{1,\text{III}}(-l)\rangle = -\gamma\,\psi_{k-1,\text{I}}^-\langle\vartheta_0(l)\, \overset{\nearrow}{Q}_{1,\text{III}}(-\gamma l)\rangle,$$

$$\psi_{k,\text{IV}}^+ \langle \overset{\nearrow}{Q}_{1,\text{IV}}(-l)\rangle = -\gamma^{-1}\psi_{k-1,\text{I}}^-\langle\varkappa(l)\, \overset{\nearrow}{Q}_{1,\text{IV}}(-\gamma^{-1}l) e^{-ilH}\rangle, \qquad (A2)$$

where

$$\overset{\nearrow}{Q}_{1,\text{III}}(-l) = -\frac{(\widehat{U} * \widehat{\chi}_1)(-l)}{4i\pi^2 l}, \quad \overset{\nearrow}{Q}_{1,\text{IV}}(-l) = -\frac{e^{-ilH}}{4i\pi^2 l}(\widehat{U} * \widehat{\chi}_2)(-l),$$

$$\varkappa(l) = \exp\left(il\gamma^{-1}(h\tan\alpha - H)(1-\gamma)\right). \qquad (A3)$$

Solutions for the second standing wave are of the form

$$\sigma_{\text{III}}^+ = \sum_{j=1}^{\infty} \sigma_{j,\text{III}}^+ \langle \overset{\nearrow}{R}_{1,\text{III}}(-l)\rangle, \quad \sigma_{\text{IV}}^+ = \sum_{j=1}^{\infty} \sigma_{j,\text{IV}}^+ \langle \overset{\nearrow}{R}_{1,\text{IV}}(-l)\rangle,$$

$$\sigma_{1,\text{III}}^+ \langle \overset{\nearrow}{R}_{1,\text{III}}(-l)\rangle = \int_0^{+\infty} \overset{\nearrow}{R}_{1,\text{III}}(-l) e^{ilx\tan\theta} e^{-ilz} dl$$

$$+ \int_0^{+\infty} \gamma\,\vartheta_0(l)\, \overset{\nearrow}{R}_{1,\text{III}}(-\gamma l) e^{-ilx\tan\theta}(e^{ilz} - e^{-ilz}e^{2ilH}) dl, \qquad (A4)$$

$$\sigma_{1,\text{IV}}^+ \langle \overset{\nearrow}{R}_{1,\text{IV}}(-l)\rangle = -\int_0^{+\infty} \overset{\nearrow}{R}_{1,\text{IV}}(-l) e^{ilx\tan\theta}(e^{il(z-H)} - e^{-il(z-H)}) dl$$

$$+ \int_0^{+\infty} \gamma^{-1}\varkappa(l)\, \overset{\nearrow}{R}_{1,\text{IV}}(-\gamma^{-1}l) e^{-ilx\tan\theta} e^{il(z-H)} dl,$$

$$\sigma_{k,\text{III}}^+ \langle \overset{\nearrow}{R}_{1,\text{III}}(-l)\rangle = -\gamma\,\sigma_{k-1,\text{I}}^-\langle\vartheta_0(l)\, \overset{\nearrow}{R}_{1,\text{III}}(-\gamma l)\rangle,$$

$$\sigma_{k,\text{IV}}^+ \langle \overset{\nearrow}{R}_{1,\text{IV}}(-l)\rangle = -\gamma^{-1}\sigma_{k-1,\text{I}}^-\langle\varkappa(l)\, \overset{\nearrow}{R}_{1,\text{IV}}(-\gamma^{-1}l) e^{-ilH}\rangle, \qquad (A5)$$

with

$$\overrightarrow{R}_{1,\mathrm{III}}\,(-l) = -\frac{(\widehat{W}_\varepsilon^+ * \widehat{\chi}_1)(-l)}{4i\pi^2 l}, \quad \overrightarrow{R}_{1,\mathrm{IV}}\,(-l) = -\frac{e^{-ilH}}{4i\pi^2 l}(\widehat{W}_\varepsilon^+ * \widehat{\chi}_2)(-l). \qquad (A6)$$

2. Cases V and VI

Functions ψ_V^+ and ψ_VI^+ must satisfy boundary conditions:

$$(\psi_\mathrm{V}^+)_z|_{x=0} = \frac{1}{4\pi^2}\int_0^{+\infty}(\widehat{U} * \widehat{\chi}_4)(-l)e^{-ilz}dl + S_{\mathrm{V,mov}}(z), \quad (\psi_\mathrm{V}^+)_x|_{z=0} = S_{\mathrm{V,bot}}(x),$$

$$(\psi_\mathrm{V}^+)_x|_{z=H} = S_{\mathrm{V,top}}(x), \quad \{(\psi_\mathrm{V}^+)_z\tan\alpha - (\psi_\mathrm{V}^+)_x\}|_{z=\tan\alpha(h-x)} = S_{\mathrm{V,inc}}(x,z)|_{z=\tan\alpha(h-x)},$$

and

$$(\psi_\mathrm{VI}^+)_z|_{x=0} = \frac{1}{4\pi^2}\int_0^{+\infty}(\widehat{U} * \widehat{\chi}_5)(-l)e^{-ilz}dl + S_{\mathrm{VI,mov}}(z), \quad (\psi_\mathrm{VI}^+)_x|_{z=0} = S_{\mathrm{IV,bot}}(x),$$

$$(\psi_\mathrm{VI}^+)_x|_{z=H} = S_{\mathrm{IV,top}}(x), \quad \{(\psi_\mathrm{VI}^+)_z\tan\alpha - (\psi_\mathrm{VI}^+)_x\}|_{z=\tan\alpha(h-x)} = S_{\mathrm{IV,inc}}(x,z)|_{z=\tan\alpha(h-x)},$$

correspondingly, where χ_4 and χ_5 are characteristic functions of intervals $[z_3, z_4]$ and $[z_4, z_5]$. Then, the solutions are

$$\psi_\mathrm{V}^+\langle\overrightarrow{Q}_{1,\mathrm{V}}\,(-l)\rangle = \sum_{j=0}^\infty \psi_{j,\mathrm{V}}^+\langle\overrightarrow{Q}_{1,\mathrm{V}}\,(-l)\rangle, \quad \psi_\mathrm{VI}^+\langle\overrightarrow{Q}_{1,\mathrm{VI}}\,(-l)\rangle = \sum_{j=0}^\infty \psi_{j,\mathrm{VI}}^+\langle\overrightarrow{Q}_{1,\mathrm{VI}}\,(-l)\rangle,$$

$$\psi_{1,\mathrm{V}}^+\langle\overrightarrow{Q}_{1,\mathrm{V}}\,(-l)\rangle = -\int_0^{+\infty}\overrightarrow{Q}_{1,\mathrm{V}}\,(-l)e^{ilx\tan\theta}(e^{il(z-H)} - e^{-il(z-H)})dl$$

$$+ \int_0^{+\infty}\gamma^{-1}\varkappa(l)\overrightarrow{Q}_{1,\mathrm{V}}\,(-\gamma^{-1}l)e^{-3ilH}e^{-ilx\tan\theta}(e^{ilz} - e^{-ilz}e^{2ilH})dl$$

$$+ \int_0^{+\infty}\gamma^{-1}\varkappa(l)\overrightarrow{Q}_{1,\mathrm{V}}\,(-\gamma^{-1}l)e^{-ilx\tan\theta}e^{il(z-H)}dl, \qquad (A7)$$

$$\psi_{1,\mathrm{VI}}^+\langle\overrightarrow{Q}_{1,\mathrm{VI}}\,(-l)\rangle = -\int_0^{+\infty}\overrightarrow{Q}_{1,\mathrm{VI}}\,(-l)e^{ilx\tan\theta}(e^{il(z-H)} - e^{-il(z-H)})dl$$

$$+ \int_0^{+\infty}\overrightarrow{Q}_{1,\mathrm{VI}}\,(-l)e^{-ilH}e^{ilx\tan\theta}e^{-ilz}dl$$

$$+ \int_0^{+\infty}\gamma\vartheta_0(l)\overrightarrow{Q}_{1,\mathrm{VI}}\,(-\gamma l)e^{-\gamma ilH}e^{-ilx\tan\theta}(e^{ilz} - e^{-ilz}e^{2ilH})dl$$

$$\psi_{k,\mathrm{V}}^+\langle\overrightarrow{Q}_{1,\mathrm{V}}\,(-l)\rangle = -\gamma^{-1}\psi_{k-1,\mathrm{I}}^-\langle\varkappa(l)\overrightarrow{Q}_{1,\mathrm{V}}\,(-\gamma^{-1}l)e^{-3ilH}\rangle$$

$$\psi_{k,\mathrm{VI}}^+\langle\overrightarrow{Q}_{1,\mathrm{VI}}\,(-l)\rangle = -\gamma\psi_{k-1,\mathrm{I}}^-\langle\vartheta_0(l)\overrightarrow{Q}_{1,\mathrm{VI}}\,(-\gamma l)e^{-\gamma ilH}\rangle, \qquad (A8)$$

where

$$\overrightarrow{Q}_{1,\mathrm{V}}\,(-l) = -\frac{e^{-ilH}}{4i\pi^2 l}(\widehat{U} * \widehat{\chi}_4)(-l), \quad \overrightarrow{Q}_{1,\mathrm{VI}}\,(-l) = -\frac{e^{-ilH}}{4i\pi^2 l}(\widehat{U} * \widehat{\chi}_5)(-l).$$

Solutions for the second standing wave are of the form

$$\sigma_{\mathrm{V}}^{+}\langle \overset{\nearrow}{R}_{1,\mathrm{V}}(-l)\rangle = \sum_{j=0}^{\infty}\sigma_{j,\mathrm{V}}^{+}\langle \overset{\nearrow}{R}_{1,\mathrm{V}}(-l)\rangle, \quad \sigma_{\mathrm{VI}}^{+}\langle \overset{\nearrow}{R}_{1,\mathrm{VI}}(-l)\rangle = \sum_{j=0}^{\infty}\sigma_{j,\mathrm{VI}}^{+}\langle \overset{\nearrow}{R}_{1,\mathrm{VI}}(-l)\rangle,$$

$$\sigma_{1,\mathrm{V}}^{+}\langle \overset{\nearrow}{R}_{1,\mathrm{V}}(-l)\rangle = -\int_{0}^{+\infty}\overset{\nearrow}{R}_{1,\mathrm{V}}(-l)e^{ilx\tan\theta}(e^{il(z-H)}-e^{-il(z-H)})dl$$

$$+\int_{0}^{+\infty}\gamma^{-1}\varkappa(l)\overset{\nearrow}{R}_{1,\mathrm{V}}(-\gamma^{-1}l)e^{-3ilH}e^{-ilx\tan\theta}(e^{ilz}-e^{-ilz}e^{2ilH})dl$$

$$+\int_{0}^{+\infty}\gamma^{-1}\varkappa(l)\overset{\nearrow}{R}_{1,\mathrm{V}}(-\gamma^{-1}l)e^{-ilx\tan\theta}e^{il(z-H)}dl, \tag{A9}$$

$$\sigma_{1,\mathrm{VI}}^{+}\langle \overset{\nearrow}{R}_{1,\mathrm{VI}}(-l)\rangle = -\int_{0}^{+\infty}\overset{\nearrow}{R}_{1,\mathrm{VI}}(-l)e^{ilx\tan\theta}(e^{il(z-H)}-e^{-il(z-H)})dl$$

$$+\int_{0}^{+\infty}\overset{\nearrow}{R}_{1,\mathrm{VI}}(-l)e^{-ilH}e^{ilx\tan\theta}e^{-ilz}dl$$

$$+\int_{0}^{+\infty}\gamma\vartheta_{0}(l)\overset{\nearrow}{R}_{1,\mathrm{VI}}(-\gamma l)e^{-\gamma ilH}e^{-ilx\tan\theta}(e^{ilz}-e^{-ilz}e^{2ilH})dl$$

$$\sigma_{k,\mathrm{V}}^{+}\langle \overset{\nearrow}{R}_{1,\mathrm{V}}(-l)\rangle = -\gamma^{-1}\sigma_{k-1,\mathrm{I}}^{-}\langle \varkappa(l)\overset{\nearrow}{R}_{1,\mathrm{V}}(-\gamma^{-1}l)e^{-3ilH}\rangle$$

$$\sigma_{k,\mathrm{VI}}^{+}\langle \overset{\nearrow}{R}_{1,\mathrm{VI}}(-l)\rangle = -\gamma\sigma_{k-1,\mathrm{I}}^{-}\langle \vartheta_{0}(l)\overset{\nearrow}{R}_{1,\mathrm{VI}}(-\gamma l)e^{-\gamma ilH}\rangle, \tag{A10}$$

with

$$\overset{\nearrow}{R}_{1,\mathrm{V}}(-l) = -\frac{e^{-ilH}}{4i\pi^{2}l}(\widehat{W}_{\varepsilon}^{+}*\widehat{\chi}_{4})(-l), \quad \overset{\nearrow}{R}_{1,\mathrm{VI}}(-l) = -\frac{e^{-ilH}}{4i\pi^{2}l}(\widehat{W}_{\varepsilon}^{+}*\widehat{\chi}_{5})(-l).$$

3. Singular case II

In this subsection, we deal with the completely defocusing case, when the spectrum $U(z)\chi_{3}(z)$, defined on the interval $[z_{2}, z_{3}]$ only, is mapped onto the whole interval $[z_{0}, z_{5}]$ by one beam cycle. The corresponding solution ψ_{II}^{+} is sought in the form

$$\psi_{\mathrm{II}}^{+} = \sum_{k=1}^{\infty}\psi_{k,\mathrm{II}}^{+}, \quad \psi_{k,\mathrm{II}}^{+}(x,z) = \int_{0}^{+\infty}e^{ilx\tan\theta}\{\overset{\searrow}{Q}_{k,\mathrm{II}}(l)e^{il(z-H)}+\overset{\nearrow}{Q}_{k,\mathrm{II}}(-l)e^{-il(z-H)}\}dl$$

$$+\int_{0}^{+\infty}e^{-ilx\tan\theta}\{\overset{\swarrow}{Q}_{k,\mathrm{II}}(l)e^{il(z-H)}+\overset{\nwarrow}{Q}_{k,\mathrm{II}}(-l)e^{-il(z-H)}\}dl. \tag{A11}$$

Now, substitute this formula to the corresponding boundary conditions:

$$(\psi_{\mathrm{II}}^{+})_{x}|_{z=0} = S_{\mathrm{II,bot}}(x), \quad (\psi_{\mathrm{II}}^{+})_{x}|_{z=H} = S_{\mathrm{II,top}}(x), \tag{A12}$$

$$(\psi_{\mathrm{II}}^{+})_{z}\tan\alpha - (\psi_{\mathrm{II}}^{+})_{x}|_{z=\tan\alpha(h-x)} = S_{\mathrm{II,inc}}(x,z)|_{z=\tan\alpha(h-x)}, \tag{A13}$$

$$(\psi_{\mathrm{II}}^{+})_{z}|_{x=0} = \frac{1}{4\pi^{2}}\int_{0}^{+\infty}(\widehat{U}*\widehat{\chi}_{3})(-l)e^{-ilz}dl + S_{\mathrm{II,mov}}(z). \tag{A14}$$

Let us define all spectra phenomenologically:

$$\overset{\searrow}{Q}_{k,\mathrm{II}}(l) = -\overset{\nearrow}{Q}_{k,\mathrm{II}}(-l), \quad \overset{\nwarrow}{Q}_{k,\mathrm{II}}(l) = \gamma^{-1}\varkappa(l)\,\overset{\nearrow}{Q}_{k,\mathrm{II}}(-\gamma^{-1}l), \tag{A15}$$

$$\overset{\nwarrow}{Q}_{k,\mathrm{II}}(-l) = -\gamma^{-1}\varkappa(l)\,\overset{\nearrow}{Q}_{k,\mathrm{II}}(-\gamma^{-1}l)e^{-2ilH}, \quad k = 1, 2, \ldots, \tag{A16}$$

$$\overset{\nearrow}{Q}_{1,\mathrm{II}}(-l) = -\frac{e^{-ilH}}{4i\pi^2 l}(\widehat{U} * \widehat{\chi}_3)(-l), \quad \overset{\nearrow}{Q}_{k,\mathrm{II}}(-l) = -\overset{\searrow}{Q}_{k-1,\mathrm{II}}(-l), \quad k = 2, 3, \ldots. \tag{A17}$$

Since the interval $[z_2, z_3]$ is mapped onto the whole interval $[z_0, z_5]$, then one can easily see that functions

$$\int_0^{+\infty} il\,\overset{\nwarrow}{Q}_{k,\mathrm{II}}(-l)e^{-il(z-H)}dl, \quad k = 1, 2, \ldots \tag{A18}$$

have nonzero values on the whole interval $[z_0, z_5]$. It means that one should decompose these functions on corresponding intervals and consider all five cases. Specifically, let us define functions $U_k(z)$ as follows:

$$U_k(z) = \frac{1}{2\pi}\int_{-\infty}^{+\infty}\widehat{U}_k(l)e^{ilz}dl, \quad \widehat{U}_k(l) = -2i\pi l\,\overset{\nwarrow}{Q}_{k,\mathrm{II}}(l)e^{-ilH}, \quad k = 1, 2, \ldots. \tag{A19}$$

Then U_k must be represented as

$$\int_0^{+\infty} il\,\overset{\nwarrow}{Q}_{k,\mathrm{II}}(-l)e^{-il(z-H)}dl = \sum_{j=1}^{5}\frac{1}{4\pi^2}\int_0^{+\infty}(\widehat{U}_k * \widehat{\chi}_j)(-l)e^{-ilz}dl, \quad k = 1, 2, \ldots. \tag{A20}$$

Thus, one should restrict the second equality in Eq. (A17) on the interval $[z_2, z_3]$:

$$\overset{\nearrow}{Q}_{k,\mathrm{II}}(-l) = -\frac{e^{-ilH}}{4i\pi^2 l}(\widehat{U}_{k-1} * \widehat{\chi}_3)(-l), \quad k = 2, 3, \ldots. \tag{A21}$$

The remaining part of the spectrum propagates according to the previous cases. Therefore, for all $k = 2, 3, \ldots$, we have

$$\psi_{k,\mathrm{II}}^+\langle\overset{\nearrow}{Q}_{1,\mathrm{II}}(-l)\rangle = \int_0^{+\infty}\frac{e^{-ilH}}{4i\pi^2 l}(\widehat{U}_{k-1} * \widehat{\chi}_3)(-l)(e^{il(z-H)} - e^{-il(z-H)})e^{ilx\tan\theta}dl$$

$$- \int_0^{+\infty}\varkappa(l)\frac{e^{-il\gamma^{-1}H}}{4i\pi^2 l}(\widehat{U}_{k-1} * \widehat{\chi}_3)(-\gamma^{-1}l)(e^{il(z-H)} - e^{-il(z-H)}e^{-2ilH})e^{-ilx\tan\theta}dl$$

$$- \psi_{\mathrm{III}}^+\left\langle\frac{1}{4i\pi^2 l}(\widehat{U}_{k-1} * \widehat{\chi}_1)(-l)\right\rangle - \psi_{\mathrm{IV}}^+\left\langle\frac{e^{-ilH}}{4i\pi^2 l}(\widehat{U}_{k-1} * \widehat{\chi}_2)(-l)\right\rangle$$

$$- \psi_{\mathrm{V}}^+\left\langle\frac{e^{-ilH}}{4i\pi^2 l}(\widehat{U}_{k-1} * \widehat{\chi}_4)(-l)\right\rangle - \psi_{\mathrm{VI}}^+\left\langle\frac{e^{-ilH}}{4i\pi^2 l}(\widehat{U}_{k-1} * \widehat{\chi}_5)(-l)\right\rangle, \tag{A22}$$

and function $\psi_{1,\mathrm{II}}^+$ is of the form

$$\psi_{1,\mathrm{II}}^+\langle\overset{\nearrow}{Q}_{1,\mathrm{II}}(-l)\rangle = \int_0^{+\infty}\frac{e^{-ilH}}{4i\pi^2 l}(\widehat{U} * \widehat{\chi}_3)(-l)(e^{il(z-H)} - e^{-il(z-H)})e^{ilx\tan\theta}dl$$

$$- \int_0^{+\infty}\varkappa(l)\frac{e^{-il\gamma^{-1}H}}{4i\pi^2 l}(\widehat{U} * \widehat{\chi}_3)(-\gamma^{-1}l)(e^{il(z-H)} - e^{-il(z-H)}e^{-2ilH})e^{-ilx\tan\theta}dl. \tag{A23}$$

In the formula Eq. (A22), spectrum $\overset{\nearrow}{Q}_{1,\mathrm{II}}(-l)$ is hidden in $\widehat{U}_{k-1}$ for all $k = 2, 3, \ldots$ via the relations Eqs. (A15)–(A17), and (A19). Now, to find explicit relations for source-type terms, one should substitute the solution obtained back into boundary conditions Eqs. (A12)–(A14).

Solution for the second standing wave is of the form

$$
\sigma_{k,\mathrm{II}}^{+} \langle \overset{\nearrow}{R}_{1,\mathrm{II}}(-l) \rangle = \int_{0}^{+\infty} \frac{e^{-ilH}}{4i\pi^2 l} (\widehat{W}_{k-1} * \widehat{\chi}_3)(-l)(e^{il(z-H)} - e^{-il(z-H)})e^{ilx\tan\theta} dl
$$
$$
- \int_{0}^{+\infty} \varkappa(l) \frac{e^{-il\gamma^{-1}H}}{4i\pi^2 l} (\widehat{W}_{k-1} * \widehat{\chi}_3)(-\gamma^{-1}l)(e^{il(z-H)} - e^{-il(z-H)}e^{-2ilH})e^{-ilx\tan\theta} dl
$$
$$
- \sigma_{\mathrm{III}}^{+} \left\langle \frac{1}{4i\pi^2 l} (\widehat{W}_{k-1} * \widehat{\chi}_1)(-l) \right\rangle - \sigma_{\mathrm{IV}}^{+} \left\langle \frac{e^{-ilH}}{4i\pi^2 l} (\widehat{W}_{k-1} * \widehat{\chi}_2)(-l) \right\rangle
$$
$$
- \sigma_{\mathrm{V}}^{+} \left\langle \frac{e^{-ilH}}{4i\pi^2 l} (\widehat{W}_{k-1} * \widehat{\chi}_4)(-l) \right\rangle - \sigma_{\mathrm{VI}}^{+} \left\langle \frac{e^{-ilH}}{4i\pi^2 l} (\widehat{W}_{k-1} * \widehat{\chi}_5)(-l) \right\rangle \tag{A24}
$$

for $k = 2, 3, \ldots$ and

$$
\sigma_{1,\mathrm{II}}^{+} \langle \overset{\nearrow}{R}_{1,\mathrm{II}}(-l) \rangle = \int_{0}^{+\infty} \frac{e^{-ilH}}{4i\pi^2 l} (\widehat{W}_{\varepsilon}^{+} * \widehat{\chi}_3)(-l)(e^{il(z-H)} - e^{-il(z-H)})e^{ilx\tan\theta} dl
$$
$$
- \int_{0}^{+\infty} \varkappa(l) \frac{e^{-il\gamma^{-1}H}}{4i\pi^2 l} (\widehat{W}_{\varepsilon}^{+} * \widehat{\chi}_3)(-\gamma^{-1}l)(e^{il(z-H)} - e^{-il(z-H)}e^{-2ilH})e^{-ilx\tan\theta} dl, \tag{A25}
$$

where

$$
\overset{\nearrow}{R}_{1,\mathrm{II}}(-l) = -\frac{e^{-ilH}}{4i\pi^2 l} (\widehat{W}_{\varepsilon}^{+} * \widehat{\chi}_3)(-l), \quad \overset{\nearrow}{R}_{k,\mathrm{II}}(-l) = -\overset{\nwarrow}{R}_{k-1,\mathrm{II}}(-l), \quad k = 2, 3, \ldots.
$$
$$
W_k(z) = \frac{1}{2\pi} \int_{-\infty}^{+\infty} \widehat{W}_k(l) e^{ilz} dl, \quad \widehat{W}_k(l) = -2i\pi l \, \overset{\nwarrow}{R}_{k,\mathrm{II}}(l) e^{-ilH}, \quad k = 1, 2, \ldots.
$$

[1] B. R. Sutherland, *Internal Gravity Waves* (Cambridge University Press, Cambridge, UK, 2010).

[2] T. Gerkema and J. T. F. Zimmerman, *An Introduction to Internal Waves. Lecture Notes* (Royal NIOZ, Texel, 2008).

[3] S. L. Gavrilyuk, N. I. Makarenko, and S. V. Sukhinin, *Waves in Continuous Media*, Lecture Notes in Geosystems Mathematics and Computing (Springer, Cham, 2017).

[4] F. John, The Dirichlet problem for a hyperbolic equation, Am. J. Math. **63**, 141 (1941).

[5] R. A. Aleksandryan, Spectral properties of operators arising from systems of differential equations of Sobolev type, Tr. Mosk. Mat. Obs. **9**, 455 (1960) (in Russian).

[6] M. V. Fokin, Solvability of the Dirichlet problem for the vibrating string equation, Dokl. Akad. Nauk SSSR **272**, 801 (1983) [Sov. Math. - Dokl. **28**, 455 (1983)].

[7] L. R. M. Maas and F. P. A. Lam, Geometric focusing of internal waves, J. Fluid Mech. **300**, 1 (1995).

[8] L. R. M. Maas, D. Benielli, J. Sommeria, and F. P. A. Lam, Observation of an internal wave attractor in a confined, stably stratified fluid, Nature (London) **388**, 557 (1997).

[9] F. P. A. Lam and L. R. M. Maas, Internal wave focusing revisited; a reanalysis and new theoretical links, Fluid Dyn. Res. **40**, 95 (2008).

[10] L. R. M. Maas, Exact analytic self-similar solution of a wave attractor field, Physica D **238**, 502 (2009).

[11] F. Beckebanze and G. Keady, On functional equations leading to exact solutions for standing internal waves, Wave Motion **60**, 181 (2016).

[12] F. Beckebanze, C. Brouzet, I. N. Sibgatullin, and L. R. M. Maas, Damping of quasi-two-dimensional internal wave attractors by rigid-wall friction, J. Fluid Mech. **841**, 614 (2018).

[13] G. Davis, T. Dauxois, T. Jamin, and S. Joubaud, Energy budget in internal wave attractor experiments, J. Fluid Mech. **880**, 743 (2019).

[14] N. H. Thomas and T. N. Stevenson, A similarity solution for viscous internal waves, J. Fluid Mech. **54**, 495 (1972).

[15] M. Rieutord, B. Georgeot, and L. Valdettaro, Inertial waves in a rotating spherical shell: Attractors and asymptotic spectrum, J. Fluid Mech. **435**, 103 (2001).

[16] G. I. Ogilvie, Wave attractors and the asymptotic dissipation rate of tidal disturbances, J. Fluid Mech. **543**, 19 (2005).

[17] J. He, B. Favier, M. Rieutord, and S. L. Dizès, Internal shear layers in librating spherical shells: The case of periodic characteristic paths, J. Fluid Mech. **939**, A3 (2022).

[18] C. Brouzet, Internal wave attractors: From geometrical focusing to non-linear energy cascade and mixing, Ph.D. thesis, Université de Lyon, 2016.

[19] H. Scolan, E. Ermanyuk, and T. Dauxois, Nonlinear Fate of Internal Wave Attractors, Phys. Rev. Lett. **110**, 234501 (2013).

[20] N. Grisouard, C. Staquet, and I. Pairaud, Numerical simulation of a two-dimensional internal wave attractor, J. Fluid Mech. **614**, 1 (2008).

[21] C. Brouzet, E. Ermanyuk, S. Joubaud, I. Sibgatullin, and T. Dauxois, Energy cascade in internal-wave attractors, Europhys. Lett. **113**, 44001 (2016).

[22] G. Davis, T. Jamin, J. Deleuze, S. Joubaud, and T. Dauxois, Succession of Resonances to Achieve Internal Wave Turbulence, Phys. Rev. Lett. **124**, 204502 (2020).

[23] F. Beckebanze, K. M. Grayson, L. R. M. Maas, and S. B. Dalziel, Experimental evidence of internal wave attractor signatures hidden in large-amplitude multi-frequency wave fields, J. Fluid Mech. **915**, A41 (2021).

[24] J. Hazewinkel, P. V. Breevoort, S. B. Dalziel, and L. R. M. Maas, Observations on the wavenumber spectrum and evolution of an internal wave attractor, J. Fluid Mech. **598**, 373 (2008).

[25] M. J. Mercier, D. Martinand, M. Mathur, L. Gostiaux, T. Peacock, and T. Dauxois, New wave generation, J. Fluid Mech. **657**, 308 (2010).

[26] T. E. Dobra, A. G. Lawrie, and S. B. Dalziel, Harmonics from a magic carpet, J. Fluid Mech. **911**, A29 (2021).

[27] S. L. Sobolev, On a problem of mathematical physics, Izv. Akad. Nauk SSSR, Ser. Mat. **18**, 3 (1954) (in Russian).

[28] T. I. Zelenyak, *Selected Problems of the Qualitative Theory of Partial Differential Equations* (Novosibirsk State University, Novosibirsk, 1970) (in Russian).

[29] M. V. Fokin, Hamiltonian systems in the theory of small oscillations of a rotating ideal fluid. I, Mat. Tr. **4**, 155 (2001) [Siberan Advan. Math. **12**, 1 (2002)].

[30] M. V. Fokin, Hamiltonian systems in the theory of small oscillations of a rotating ideal fluid. II, Mat. Tr. **5**, 167 (2002) [Siberian Advan. Math. **12**, 1 (2002)].

[31] S. D. Troitskaya, Mathematical analysis of inertial waves in rectangular basins with one sloping boundary, Stud. Appl. Math. **139**, 434 (2017).

[32] Y. C. D. Verdiere and L. Saint-Raymond, Attractors for two-dimensional waves with homogeneous hamiltonians of degree 0, Commun. Pure Appl. Math. **73**, 421 (2020).

[33] S. Dyatlov, J. Wang, and M. Zworski, Mathematics of internal waves in a 2D aquarium, arXiv:2112.10191.

[34] A. Tabaei and T. R. Akylas, Nonlinear internal gravity wave beams, J. Fluid Mech. **482**, 141 (2003).

[35] K. G. Lamb, Nonlinear interaction among internal wave beams generated by tidal flow over supercritical topography, Geophys. Res. Lett. **31**, L09313 (2004).

[36] A. Tabaei, T. R. Akylas, and K. G. Lamb, Nonlinear effects in reflecting and colliding internal wave beams, J. Fluid Mech. **526**, 217 (1999).

[37] T. Gerkema, Internal-wave reflection from uniform slopes: Higher harmonics and coriolis effects, Nonlinear Processes Geophys. **13**, 265 (2006).

[38] T. Kataoka and T. R. Akylas, Stability of internal gravity wave beams to three-dimensional modulations, J. Fluid Mech. **736**, 67 (2013).

[39] H. Karimi and T. R. Akylas, Parametric subharmonic instability of internal waves: Locally confined beams versus monochromatic wavetrains, J. Fluid Mech. **757**, 381 (2014).

[40] T. Kataoka and T. R. Akylas, On three-dimensional internal gravity wave beams and induced large-scale mean flows, J. Fluid Mech. **769**, 621 (2015).

[41] H. H. Karimi and T. R. Akylas, Near-inertial parametric subharmonic instability of internal wave beams, Phys. Rev. Fluids **2**, 074801 (2017).

[42] B. Fan, T. Kataoka, and T. R. Akylas, On the interaction of an internal wavepacket with its induced mean flow and the role of streaming, J. Fluid Mech. **838**, R1 (2018).

[43] F. Beckebanze, K. J. Raja, and L. R. M. Maas, Mean flow generation by three-dimensional nonlinear internal wave beams, J. Fluid Mech. **864**, 303 (2019).

[44] T. Kataoka and T. R. Akylas, On mean flow generation due to oblique reflection of internal waves at a slope, Stud. Appl. Math. **142**, 419 (2019).

[45] B. Fan and T. R. Akylas, Finite-amplitude instabilities of thin internal wave beams: experiments and theory, J. Fluid Mech. **904**, A16 (2020).

[46] S. A. Gabov and A. G. Sveshnikov, *Problems in the Dynamics of Stratified Fluids* (Izdatel Nauka, Moscow, 1986) (in Russian).

[47] S. G. L. Smith and W. R. Young, Tidal conversion at a very steep ridge, J. Fluid Mech. **495**, 175 (2003).

[48] F. Pétrélis, S. G. L. Smith, and W. R. Young, Tidal conversion at a submarine ridge, J. Phys. Oceanogr. **36**, 1053 (2006).

[49] P. G. Baines, The reflexion of internal/inertial waves from bumpy surfaces, J. Fluid Mech. **46**, 273 (1971).

[50] B. Voisin, Near-field internal wave beams in two dimensions, J. Fluid Mech. **900**, A3 (2020).

[51] H. Sandstrom, On topographic generation and coupling of internal waves, Geophys. Astrophys. Fluid Dyn. **7**, 231 (1975).

[52] P. Fischer and E. Ronquist, Spectral element methods for large scale parallel Navier–Stokes calculations, Comput. Meth. Appl. Mech. Engng. **116**, 69 (1994).

[53] P. F. Fischer and J. S. Mullen, Filter-based stabilization of spectral element methods, C. R. Acad. Sci. Paris I **332**, 265 (2001).

[54] G. Wang, Q. Zheng, M. Lin, and F. Qiao, Three dimensional simulation of internal wave attractors in the Luzon strait, Acta Oceanol. Sinica **34**, 14 (2015).

[55] Y. Guo and M. Holmes-Cerfon, Internal wave attractors over random, small-amplitude topography, J. Fluid Mech. **787**, 148 (2016).

[56] G. V. Virabyan, On the resolvent of an operator, Dokl. Akad. Nauk SSSR **151**, 258 (1963) [Sov. Math. **4**, 970 (1963)].